VAULT REFERENCE COPY

UCRL-52523

A ONE-DIMENSIONAL MODEL FOR IN SITU COAL GASIFICATION

C. B. Thorsness, E. A. Grens, and A. Sherwood

August 25, 1978

Work performed under the auspices of the U.S. Department of Energy by the UCLLL under contract number W-7405-ENG-48.

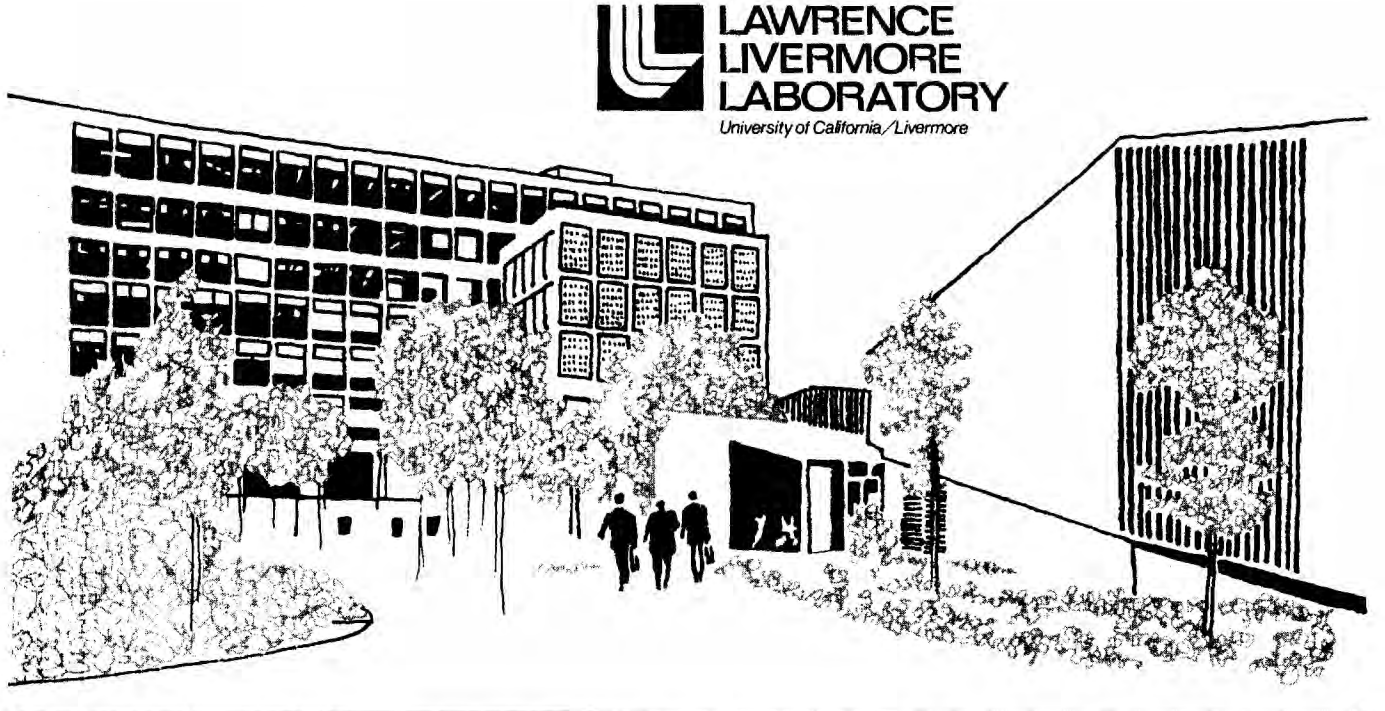

DISCLAIMER

This document was prepared as an account of work sponsored by an agency of the United States Government. Neither the United States Government nor the University of California nor any of their employees, makes any warranty, express or implied, or assumes any legal liability or responsibility for the accuracy, completeness, or usefulness of any information, apparatus, product, or process disclosed, or represents that its use would not infringe privately owned rights. Reference herein to any specific commercial product, process, or service by trade name, trademark, manufacturer, or otherwise, does not necessarily constitute or imply its endorsement, recommendation, or favoring by the United States Government or the University of California. The views and opinions of authors expressed herein do not necessarily state or reflect those of the United States Government or the University of California, and shall not be used for advertising or product endorsement purposes.

Distribution Category
UC-90C

LAWRENCE LIVERMORE LABORATORY
University of California/Livermore, California/94550

UCRL-52523

A ONE-DIMENSIONAL MODEL FOR IN SITU COAL GASIFICATION

C. B. Thorsness, E. A. Grens, and A. Sherwood

MS. date: August 25, 1978

CONTENTS

Abstract 1
Introduction 1
Model Equations 2
  Thermal Balances 2
  Mass Balances 4
  Equation of State 4
  Momentum-Balance Equation 4
Physical and Chemical Models 5
  Permeability-Particle Size Correlation 5
  Thermal Conductivity 6
  Interphase Transport Coefficients 7
  Reaction Rates 8
  Thermodynamic Properties 10
Method of Solution 11
  Grid System 13
  Gas-Phase ODE's 13
  Solid-Phase Equations 15
  Hydrodynamic Equation 15
Sample Calculations 16
  Experimental Reactor Run 16
  Three Oxygen-Feeds 19
  Field Scale Run 20
Nomenclature 25
Appendix A. Coal Permeability Correlation 28
Appendix B. Stoichiometric Coefficients 30
  General Coefficients 30
  Coefficients for Wyodak Coal 32
Appendix C. Rate Equations 33
Appendix D. Char Thermodynamics 38
Appendix E. Variable Zoning 40
  Rate Criteria 40
  Temperature Gradient Criteria 40
  Pressure Criteria 41
Appendix F. Finite Difference Representations 42
  Gas-Phase Equations in Large Zones 42
  Solid-Phase Equations 43
Appendix G. Test Problems 45
  Heat Wave 45
  Catalyst Regeneration 47
References 51

A ONE-DIMENSIONAL MODEL FOR IN SITU COAL GASIFICATION

ABSTRACT

This report presents a calculational model that describes certain aspects of the in situ gasification process. The primary aim of this preliminary work was to predict and correlate reaction and thermal-front propagation rates and product-gas composition as a function of coal bed properties and process operating conditions.

We restricted our initial efforts to a one-dimensional transient Darcy flow in a permeable packed bed. The numerical calculations include a detailed description of the reacting system chemistry (13 species), with appropriate reaction rates and overall heat and mass transport in the system.

A comparison of calculated results with experimental data from a packed-bed combustion tube showed good agreement for reaction-zone propagation rates and produced-gas compositions. However, we believe the sensitivity of the calculations to other reaction-rate and transport-coefficient models needs to be investigated.

INTRODUCTION

We have developed a relatively simple model for the coal gasification process in fixed, permeable coal beds. The model is transient and one-dimensional and includes time and distance changes in process variables in the principal direction of the gas flow. Variations in the two orthogonal directions are not considered. The model, when used in laboratory experiments, determines the influence of changes in operating conditions on the course of gasification. The model may also be of assistance in using results of short, laboratory-scale, runs to predict performance of much longer, field-scale, systems. This report documents the essential features of the model and presents some sample calculations.

The model predicts the reaction-front propagation-rate and gas-product composition for given injection gas-flow rates and compositions. Gas, solid temperatures, and composition profiles in time and distance are also determined. These results are obtained by solving 12-species mass balances, energy balances on gas and solid phases, and a Darcy-flow momentum equation. The equations are coupled by source/sink terms involving heat and mass generation from eleven chemical reactions. Reactions include four heterogeneous gas/char reactions, the water-gas shift reaction, coal pyrolysis, coal drying, steam condensation/vaporization, and three possible gas-phase oxidation reactions. Reaction rates are determined by chemical kinetics at low temperatures and are limited by mass transfer at higher temperatures. Most of the reactions are potentially limited by equilibrium considerations, excepting pyrolysis and oxidation which are considered irreversible. Solid heat conduction is included along with gas/solid heat transfer.

Because of limitations imposed by the one-dimensional framework and lack of information, several phenomena that may be very important for in situ gasification are not considered in this model. These include the effects of: tar condensation and plugging, gas losses to surroundings, water intrusion from surroundings, heat losses, and coal-bed movement as a result of shrinking (or swelling) during drying and pyrolysis. The model can be extended to include in approximate fashion some of these effects, but this would require very careful consideration of how these essentially two- (or three-) dimensional phenomena might be represented in one dimension.

The solution of the model equations is implemented by a modular FORTRAN computer program. The modular feature allows a change in specification of the numerous physical and chemical phenomena to be made with a minimum of effort. The solution procedure incorporates a quasi-steady state approximation for changes associated with the gas phase. This represents a recognition that the gas-phase mass and heat capacities are small, and thus the gas composition and temperture distribution are primarily determined by interaction with the coexisting solid phase. This is a different approach from that adopted by Sawyer and Shuck[1] and Winslow[2] in their one-dimensional gasification models.

Another feature incorporated into the solution procedure and not used in other gasification models is the use of an adaptive zoning scheme. This scheme rezones the grid system used in the solution as a result of changes occurring in the system. That is useful, since numerous relatively sharp fronts, associated with

rapid temperature and compositional changes in the process, continually change position. Fine zones are used near rapid changes while much coarser zones are used in areas of slow changes. This allows relatively large systems to be simulated with fewer grid locations than would be necessary with a constant grid system.

MODEL EQUATIONS

We have divided the differential equations describing the gasification process into conservation laws appropriate to the gas and solid phases. They include, in the gas phase, energy, mass, and momentum conservation; in the solid phase, only energy and mass conservation are included. The eight gas species on which balances are written include N_2, O_2, H_2O, H_2, CH_4, CO, CO_2, and "tar." The solid species are coal, char, $H_2O(M)$, $H_2O(F)$, and ash. Note that the liquid species have been grouped here and elsewhere with the solid species. $H_2O(M)$ is liquid water that is located in macroporosity and is available for flow. $H_2O(F)$ is liquid water that is present in the micropores of the coal and can only be removed by thermal or chemical means.

Thermal Balances

An enthalpy balance for the gas phase can be written in one-dimension as:

$$\phi \sum_{i=1}^{8} \left[C_i \frac{\partial h_i}{\partial t} \right] = \frac{\partial}{\partial x} \left[\phi \lambda_g \frac{\partial T}{\partial x} \right] + h_T (T_s - T)$$

$$+ \sum_{j=1}^{11} \sum_{i=1}^{8} \left[h_i a_{ij} R_j \right] - \sum_{i=1}^{8} \left[v C_i \frac{\partial h_i}{\partial x} \right] + \left[\frac{\partial (\ln \tilde{v})}{\partial (\ln T)} \right] \frac{DP}{Dt} \qquad (1)$$

where ϕ is the porosity, C_i is the molar concentration of gas species i based on the void volume, h_i is the molar enthalpy of species i (cal/mole) related to a standard state, λ_g is the thermal conductivity in the gas phase (cal/cm/s/K), T is the gas temperature (K), T_s is the solid temperature (K), h_T is the effective gas/solid heat transfer coefficient per unit volume of bed (cal/cm^3/s/K), a_{ij} are stoichiometric coefficients for reaction j, R_j is the rate of reaction j per unit volume of bed (g-mole/cm^3/s), v is the superficial gas velocity (cm/s), $\tilde{v}$ is the molar gas volume (cm^3/mole), P is pressure (atm), t is time (s), and x is the space dimension (cm). This formulation neglects thermal energy generated by fluid motion, gravitation contributions, and fluxes due to diffusive mass flow.

Similarly, the solid-phase enthalpy balance can be given by:

$$\sum_{i=1}^{5} \left[\rho_i \frac{\partial h_{s_i}}{\partial t} \right] = \frac{\partial}{\partial x} \left[(1 - \phi) \lambda_s \frac{\partial T_s}{\partial x} \right]$$

$$+ h_T (T - T_s) + \sum_{j=1}^{11} \sum_{i=1}^{5} \left[h_{s_i} a_{s_{ij}} M_i R_j \right] - \sum_{i=1}^{5} \left[v_{s_i} \rho_i \frac{\partial h_{s_i}}{\partial x} \right] \qquad (2)$$

where ρ_i is the concentration of solid species i (g/cm^3) based on the bed volume, h_{s_i} is the enthalpy of solid species i per unit weight (cal/g), λ_s is the conductivity of the solid phase, M_i is the molecular weight of solid species i, and v_{s_i} is the velocity of species i (cm/s).

These two balances have been modified in two ways to obtain the final forms used in the model. First, the source terms resulting from chemical reaction have been modified. Reactions occur both heterogeneously at a gas/solid interface and homogeneously in the gas or solid. Thermal energy released or absorbed during the course of the reaction is liberated at the point of the reaction. The initial partition of this energy between solid and gas phases depends on detailed interactions occurring at the point of reaction. The model, on the other hand, does not attempt to define such detailed interactions. Instead, the splitting of the heat generation is somewhat arbitrary and serves as only a rough approximation of the true situation. As a result, the thermal source terms are redefined so that the thermal energy release can be divided between gas and solid in any desired manner and is not tied directly to appearance or disappearance of species in one phase or the other. This is done through the following definitions:

$$\Delta H_j = \sum_{i=1}^{5} \left[h_{s_i} a_{s_{ij}} \right] + \sum_{i=1}^{8} \left[h_i a_{ij} \right], \tag{3a}$$

$$H_g = \sum_{i=1}^{11} \left[f_j \Delta H_j R_j \right], \tag{3b}$$

$$H_s = \sum_{i=1}^{11} \left[(1 - f_j) \Delta H_j R_j \right]. \tag{3c}$$

Here ΔH_j is the overall heat effect of reaction j. The heat sources H_g and H_s become the source terms to be used, respectively, in the gas and solid equations. Note: the sum of H_g and H_s is equal to the sum of the original source terms in Eqs. (1) and (2). The parameter f_j is a number between 0 and 1 that determines how the heat effect of reaction j is to be split between the gas and solid phases. Currently, reactions involving solids in some fashion, either actively or as a catalyst, are assigned values of 0, while fully homogeneous gas-phase reactions are assigned values of 1.

The second modification of Eqs. (1) and (2) includes the lumping of all conductive transport into the solid-phase balance, neglecting the accumulation term in the gas phase, and neglecting the DP/Dt term in the gas equation. Neglecting the accumulation term in the gas phase is simply part of the quasi-steady state assumption made about the behavior of the gas phase. This assumption recognizes that the convective, interphase transfer, and source terms dominate the accumulation term at all points in the system, owing to the relatively low density of the gas phase. The DP/Dt term is neglected since only mild pressure gradients are assumed to be present in the system.

Written in terms of temperature, the final form of the equations for the heat balances become, in the gas phase,

$$c_g v_g \frac{dT}{dx} = -h_T (T - T_s) - H_g, \tag{4}$$

with $T = T_o$ at $x = 0$ and $c_g = \sum_{i=1}^{8} C_i c_{p_i}$,

and, in the solid phase,

$$c_s \frac{\partial T_s}{\partial t} = \frac{\partial}{\partial x} \left[(1 - \phi) k \frac{\partial T_s}{\partial x} \right] + h_T (T - T_s) - H_s - v_s \rho_3 c_{s_3} \frac{\partial T_s}{\partial x} \tag{5}$$

with $T_s = T_{s_o} \quad 0 \leqslant X \leqslant L \quad t = 0$

$$\frac{\partial T_s}{\partial x} = 0 \quad x = 0, \text{and } L \quad t > 0$$

$$c_s = \sum_{i=1}^{5} \rho_i c_{s_i}.$$

Here c_{p_i} is the molar heat capacity at constant pressure of gas species i (cal/mole·K), and c_{s_i} is the heat capacity of solid species i (cal/gm·K). The only nonzero velocity in the solid heat balance is the mobile water phase. The gas-phase temperature equation, Eq. (4), has been reduced to a first ordinary differential equation (ODE).

Mass Balances

The eight gas balances are written as ODE's, neglecting again the accumulation terms:

$$\frac{d(vC_i)}{dx} = \sum_{j=1}^{11} \left[a_{ij} R_j \right] \tag{6}$$

with $C_i = C_{i_o}$, and $v \sum_{i=1}^{8} C_{i_o} = G$ at $x = 0$.

The solid balances are written for all species, except mobile water, as:

$$\frac{\partial \rho_i}{\partial t} = M_i \sum_{j=1}^{11} \left[a_{s_{ij}} R_j \right] \tag{7}$$

with $\rho_i = \rho_{i_o}(x)$ at $t = 0$.

For mobile water, the convective term is retained, which gives:

$$\frac{\partial \rho_3}{\partial t} = \frac{\partial (v_s \rho_3)}{\partial x} + M_3 \sum_{j=1}^{11} \left[a_{s_{3j}} R_j \right] \tag{8}$$

with $\rho_3 = \rho_{3_o}(x)$ at $t = 0$ and $\rho_3 = 0$ at $x = 0$.

Equation of State

An equation of state is required to relate gas-phase pressure, temperature, and concentration. Ideal gas behavior is assumed and is given in the current nomenclature by:

$$\frac{P}{RT} = \sum_{i=1}^{8} C_i \tag{9}$$

where R is the gas constant (cm^3·atm/g-mole·K).

Momentum-Balance Equation

In general, some type of momentum balance should be written for each flowing phase. However, in the current version of the model, the liquid-phase balance is avoided by assuming that all mobile water in

the system is moving at a constant velocity. This velocity is set arbitrarily at one-half the exhaust gas velocity. In any event, the effect of liquid water velocity is small. The momentum balance for the gas phase is replaced by Darcy's Law:

$$V = \frac{-K}{\mu} \frac{dP}{dx} \tag{10}$$

with $P = P_L$ at $x = L$ where P_L is the exhaust pressure (atm) at the exhaust end of the system, L is the system length (cm), K is the permeability (D), and μ is the viscosity (cps).

PHYSICAL AND CHEMICAL MODELS

There are a number of rates and coefficients appearing in the defining equations that require some type of model or theoretical framework for their specification. These include the gas permeability coefficient K, the effective thermal conductivity constant k, the interphase heat transfer coefficient h_T, the chemical reaction rate R_j, and various thermodynamic properties. The thermodynamic relations are rather straightforward and not subject to much debate. On the other hand, the determination of the transport coefficients and reaction rates are subject to a great deal of uncertainty. Consequently, the following represents only one of many possibilities for their specification. The reaction rate correlations are obtained from several published sources. The transport coefficients are based on models that rely primarily on the concept of a packed bed, but have been extended to give estimates for states of the system beyond those encountered in normal packed-bed operation.

Permeability-Particle Size Correlation

A simple functional relation associates permeability with porosity. This relation is then used in conjunction with the Carmen-Kozeny Equation to establish a characteristic particle size for use in other correlations.

Limited experimental evidence (see App. A) indicates that a change in permeability of a coal sample can be related to changes in porosity by:

$$\frac{K}{K_0} = \exp\left[\alpha(\phi - \phi_0)\right],$$

for $\phi < \phi_\ell$, where K_0 and ϕ_0 are, respectively, the initial permeability and porosity, α is a parameter to be chosen, and ϕ_ℓ is upper limit on porosity above which K is constant.

Using the relation between permeability, porosity, and particle size given by the Carmen-Kozeny relation

$$K \propto \frac{d^2\phi^3}{(1-\phi)^2},$$

a relation for the change in particle size can be developed:

$$\frac{d}{d_0} = \left(\frac{\phi_o}{\phi}\right)^{3/2} \exp\left[\frac{\alpha}{2}(\phi - \phi_o)\right] \tag{11}$$

for $\phi < \phi_\ell$. Here d_0 is the assumed initial characteristic particle size. Note that a factor $(1-\phi)/(1-\phi_0)$ has been dropped since it is near unity where this relation is used. The porosity ϕ_ℓ is also defined using this relation by noting that if:

$$\frac{\partial d}{\partial \phi} \leqslant 0,$$

then

$$\phi_\ell \leqslant \frac{3}{\alpha} .$$

This insures that the particle size given by Eq. (11) will always decrease as ϕ increases. It is assumed here that $\phi_\ell = 3/\alpha$.

Since estimates of d are required for $\phi < \phi_\ell$, and in some cases ϕ_0 may be greater than ϕ_ℓ, the relation is extended using the following:

Case 1. $\phi_0 < \phi$

$$\phi < \phi_\ell \quad \frac{d}{d_0} = \left(\frac{\phi_0}{\phi}\right)^{3/2} \exp\left[\frac{\alpha}{2}\ (\phi - \phi_0)\right] ,$$

$$\phi \geqslant \phi_\ell \quad \frac{d}{d_0} = z(1 - \phi)^{1/3}$$

where

$$z = d|_{\phi = \phi_\ell} (1 - \phi_\ell)^{-1/3} .$$

Case 2. $\phi_0 \geqslant \phi_\ell$

$$\frac{d}{d_0} = z(1 - \phi)^{1/3}$$

where $z = (1 - \phi_0)^{-1/3}$. This extension to cases when $\phi > \phi_\ell$ just assumes the number of particles and their shape remain constant, and the change in dimension is related to the change in solid material.

These relations are certainly not an exact representation but do tend to change in a reasonable fashion as the system evolves. Some examples of the changes in K and d with ϕ are given in Figs. 1 and 2.

Thermal Conductivity

A correlation given by Yagi and Kunii[3] is used to relate effective thermal conductivity to the state of the system. The correlation takes into account conduction in the solid, radiant transfer, and conduction through fluid adjacent to the solid. Assuming an emissivity of 0.8 for the solid, and using the values of their parameters $\beta = \gamma = 1$ and $\phi = 0.04$ (not to be confused with ϕ used herein), this gives:

$$k = \frac{1 - \phi}{(1/\lambda_s) + 1/(25\lambda_g + dL_s)} + \phi d L_v . \tag{12}$$

Here λ_s is the conductivity of the solid matrix (cal/cm/s/K), λ_g is the conductivity of the gas (cal/cm/s/K),

$$L_s = 3.16 \times 10^{-12} T_s^3 ,$$

and

$$L_v = \frac{5.4 \times 10^{-12} T_s^3}{1 - 0.125\ \phi/(1 - \phi)}$$

The computer model assumes λ_s is a constant and λ_g is only a function of the hydrogen content of the gas and its temperature. The length parameter, d, is obtained from the previously described correlation with porosity.

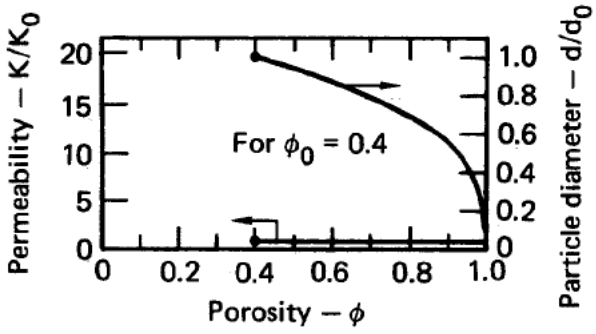

Fig. 1. Changes of K and d for a system with a large initial porosity ($\phi_0 = 0.4$).

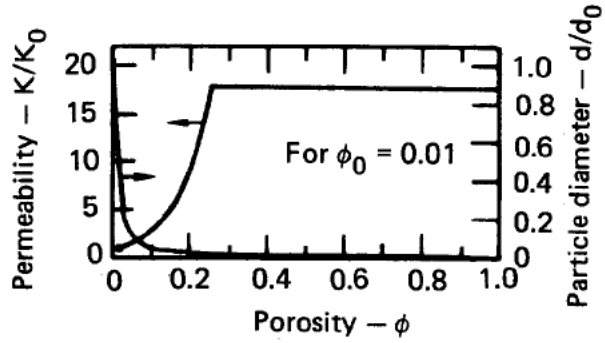

Fig. 2. Changes of K and d for a system with a small initial porosity ($\phi_0 = 0.01$).

Interphase Transport Coefficients

Estimates of both heat and mass transfer coefficients are required. A model based on a j-factor correlation given by Bird et al.[4] is used in conjunction with estimates of d given above.

Bird et al.[4] gives the following correlation for heat transfer in a packed bed:

$$\frac{h}{c_g v} (Pr)^{2/3} = 0.91\ Re^{-0.51}\ \psi \tag{13}$$

for $Re < 50$ with $Re = \frac{v}{A\nu\psi}$.

Here Ψ is a shape factor of order unity, A is the ratio of surface area to volume in the bed, Re is the Reynolds number, ν is the kinematic viscosity of the fluid (cm^2/s), and Pr is the fluid Prandtl number.

We define A based on a packed sphere model:

$$A = \frac{6\gamma(1-\phi)}{d} ,$$

where γ is a shape factor to correct for the nonspherical shape of the particles. This leads to the following for the heat transfer coefficient h_T based on a unit volume of bed:

$$h_T = hA = \frac{0.91\ C_g\ v^{0.49}\ \nu^{0.51}}{Pr^{2/3}} \left[\frac{6s(1-\phi)}{d}\right]^{1.51} \tag{14}$$

where $s = \gamma^{\Psi}$.

Currently it is assumed that $s = 1$, $Pr^{2/3} = 1$, and that the kinematic viscosity is given by:

$$\nu = \frac{3.3 \times 10^{-5} T^{3/2}}{P} .$$

This last assumption is based on average values for the gas in the system at 600 K.

An estimate of an effective interphase mass transfer coefficient is required for specification of reaction rates. A mass transfer coefficient, k_y, based on a mole fraction driving force, can be related to h_T by:

$$\frac{k_y}{h_T} = \left(\frac{Pr}{Sc}\right)^{2/3} \frac{1}{C_T} . \tag{15}$$

This relation is further simplified by assuming $(Pr/Sc)^{2/3} = 1$ and $C_T = 10$, where C_T is the total gas concentration. As a result, k_{y_T} is given simply by:

$$k_y = 0.1\ h_T . \tag{16}$$

Reaction Rates

A set of eleven reactions are used in the current model. This is by no means a unique set, but it probably imcorporates those reactions most important to the process. The rates of heterogeneous reactions and those catalyzed by surfaces are limited in the model by mass transport considerations. In general, equilibrium relations are used to limit the extent of certain reactions and to develop approximate terms for reverse rates.

The eleven reactions currently used in the model are listed in Table 1. The $a_{s_{ij}}$ and the a_{ij} are stoichiometric coefficients defined in detail in App. B. The first two reactions describe the condensation and evaporation of water. As noted earlier, $H_2O(M)$ is liquid water that is allowed to convect through the system. All condensing water vapor forms $H_2O(M)$. $H_2O(F)$ is liquid water located in small pores of the coal. It is assumed that this water can only be removed by evaporation and, once removed, cannot reappear. Thus, reaction 2 is irreversible.

Reaction 3 represents pyrolysis of the coal. The products of this reaction are numerous gaseous species and solid char. Note that here, as elsewhere, the definition of a pseudomolecule of coal or char is based, for convenience, on a molecule containing one carbon. The species C_9H_c, representing all products of pyrolysis not otherwise accounted for, is incorporated into this reaction. The hydrogen content of this fictious species is chosen to satisfy the stoichiometry of the system. Also note that N, S, and other lesser components of real coal have been omitted, and it is assumed that pyrolysis is an irreversible process.

Reactions 4-7 are heterogeneous reactions representing oxidation and various gasification reactions. Reaction 8, the water-gas shift reaction, involves only gas-phase species, but since its homogeneous rate is low at modest temperatures[5] and it is known to be highly catalyzed by certain solids,[6] it is also treated in a manner similar to reactions 4-7. All these reactions, except the oxidation one, are considered reversible and thus limited by equilibrium considerations. Those species occurring in brackets (see Table 1) are included in the reactions only to maintain a stoichiometric balance. They are not major products, and their choice is somewhat arbitrary.

Table 1. Model Chemical Reactions. (CH_aO_b = Coal, $CH_{\bar{a}}O_{\bar{b}}$ = Char, and C_9H_c = Tar.)

1)	$H_2O(M) \leftrightharpoons H_2O(g)$
2)	$H_2O(F) \rightarrow H_2O(g)$
3)	$CH_aO_b \rightarrow \lvert a_{s_{2,3}} \rvert CH_{\bar{a}}O_{\bar{b}} + \lvert a_{5,3} \rvert CH_4 + \lvert a_{3,3} \rvert H_2O(g)$
	$+ \lvert a_{6,3} \rvert CO + \lvert a_{4,3} \rvert H_2 + \lvert a_{7,3} \rvert CO_2 + \lvert a_{8,3} \rvert C_9H_c$
4)	$CH_{\bar{a}}O_{\bar{b}} + \lvert a_{2,4} \rvert O_2 \rightarrow CO_2 + [\lvert a_{3,4} \rvert H_2O(g)]$
5)	$CH_{\bar{a}}O_{\bar{b}} + \lvert a_{3,5} \rvert H_2O(g) \leftrightharpoons CO + \lvert a_{4,5} \rvert H_2$
6)	$CH_{\bar{a}}O_{\bar{b}} + \lvert a_{7,6} \rvert CO_2 \leftrightharpoons \lvert a_{6,6} \rvert CO + [\lvert a_{3,6} \rvert H_2O(g)]$
7)	$CH_{\bar{a}}O_{\bar{b}} + \lvert a_{4,7} \rvert H_2 \leftrightharpoons CH_4 + [\lvert a_{6,7} \rvert CO]$
8)	$CO + H_2O(g) \leftrightharpoons CO_2 + H_2$
9)	$2H_2 + O_2 \rightarrow 2H_2O(g)$
10)	$2CO + O_2 \rightarrow 2CO_2$
11)	$CH_4 + 2O_2 \rightarrow CO_2 + 2H_2O(g)$

Reactions 9-11 are possible homogeneous, gas-phase oxidation reactions. They are currently considered irreversible. Their primary function is to allow for more rapid consumption of oxygen than would be provided by reaction 4 alone.

The forms of the rate expressions currently used in the model have been obtained from various literature sources. The exact forms of these expressions, including mass-transport and equilibrium limitations, are given in detail in App. C. The general formulation is outlined below.

The evaporation/condensation rate, R_1, is given by a purely mass-transfer controlled expression:

$$R_1 = k_y \left(\frac{P}{\bar{P}} - y_3 \right) \tag{17}$$

where $P = \exp\left[12.61 - \frac{4690}{\tilde{T}_1}\right]$ and $\tilde{T}_1 = \beta_1 T_s + (1 - \beta_1)T$.

Here P is the vapor pressure, y_3 is the mole fraction of water in the gas phase, and $\tilde{T}_1$ is some average temperature. Currently $\beta_1 = 1$. Some additional features, including a limitation of P, are described in App. C.

The coal drying rate, R_2, is assumed to be controlled both by an external diffusion limitation implied in k_y, and by resistance internal to the coal matrix. The latter attempts to recognize that the water in the coal is distributed throughout it and is not located solely at the gas/solid interfaces. The basic rate is:

$$R_2 = k_y \frac{\gamma^2}{3\eta} \left(\left(\frac{\rho^4}{\rho_4^*} \right) \frac{P}{\bar{P}} - y_3 \right) \tag{18}$$

where $P = \exp\left[12.61 - \frac{4690}{\tilde{T}_2}\right]$ and $\tilde{T}_2 = \beta_2 T_s + (1 - \beta_2)T$.

Parameters γ and η deal with the internal resistance and ρ_4^* is the initial $H_2O(F)$ density. The parameters γ and η are developed and defined in App. C. A limiting expression for R_2 is also developed there for cases in which $\tilde{T}_2$ might exceed the saturation temperature. Currently $\beta_2 = 1$.

The heterogeneous reactions 4-8 have rates influenced by three mechanisms: mass-transport limitations from the bulk gas to the solid surface, mass-transport limitations in any internal particle porosity, and kinetic limitations at the solid surface. We assume that the internal transport and surface kinetics can be lumped into one effective chemical rate expression. (This choice is primarily a result of lack of information, as most literature results for gasification reactions do not allow these two influences to be separated.) The total rate is then obtained by considering the external transport step in series with the lumped, kinetic, internal-diffusion rate. This leads to the following expression for the overall rate R_T:

$$R_T = \frac{1}{(1/R_c) + (1/R_m)} \tag{19}$$

where R_c is the effective chemical rate evaluated using gas compositions of the bulk gas. The parameter R_m is the mass-transfer rate of a limiting reactant defined by:

$$R_m = k_y \, y_\ell \tag{20}$$

where y_ℓ is the mole fraction of the limiting reactant in the bulk gas. Equation 19 is only strictly valid for cases in which R_c is linearly dependent on y_ℓ; however, its use is adopted for all heterogeneous reactions since it is an effective means of imposing some type of external mass-transport limitation on heterogeneous reactions. The exact forms of R_c and R_m that are currently used for reactions 4-8 are given in App. C.

The effective chemical rate, R_c, for reactions 5-9 are limited by equilibrium considerations. This is incorporated into the model along with the approximate expression for reverse-reaction rates through the

use of an equilibrium constant evaluated for each reaction as a function of temperature. As an example of how this is implemented, consider reaction 8 in which a forward reaction rate is given by:

$$R^{+}_{c_8} = k^{+}_8 C_6 \; C_3$$

where k^{+}_8 is a function of temperature. It is assumed that a reverse reaction rate can be given approximately by:

$$R^{-}_{c_8} = k^{-}_8 \; C_7 \; C_4$$

Here k^{-}_8 is an unknown function of temperature. At equilibrium, the following is valid:

$$K_{E_8} = \frac{y_7 \, y_4}{y_6 \, y_3} = \frac{k^{+}_8}{k^{-}_8} \; .$$

This relation between K_{E_8} and the rate constants is extended by assuming at any composition $k^{-}_8 = k^{+}_8 / K_{E_8}$. As a result, the total rate R_c can be given as:

$$R_{c_8} = R^{+}_{c_8} - R^{-}_{c_8} = k^{+}_8 \left[C_6 \, C_3 - \frac{C_7 C_4}{K_{E_8}} \right] .$$

Note that this correctly gives a zero rate when the system is at an equilibrium state. It also allows estimates of the rates of reverse reactions to be made at any point at which the equilibrium favors the reverse reaction. The other reactions are handled in similar fashion and are given in App. C.

Thermodynamic Properties

The thermodynamic properties required for the solution include standard enthalpies and entropies of formation and heat capacities. These are used to calculate heats of reactions, equilibrium constants, and overall gas and solid heat capacities.

The heat capacities for gas and solid species are assumed to only be a function of temperature. The functional dependence used is that of a second-order polynomial for gas species and a cubic polynomial for solid species. The enthalpies used to calculate the ΔH_s and ΔH_g are given simply by:

$$h_i \, (T) = H_{f_i} + \int_{298.16}^{T} c_{p_i} \, dT \tag{21}$$

where H_{f_i} is the standard heat of formation of species i at 298.16 K.

The equilibrium constants K_{E_j} based on mole fractions are calculated in the usual fashion using:

$$K_{E_j} = K_{p_j} P^{\epsilon} \; ,$$

$$\ell n K_{p_j} = \ell n K_{p_j} \Big|_{298.16} + \int_{298.16}^{T} \frac{\Delta H_j}{RT^2} \, dT,$$

$$\ell n K_{p_j} \Big|_{298.16} = - \frac{\Delta F_j \Big|_{298.16}}{RT} \; .$$

Here ϵ is the net mole change in gas species as the reaction proceeds as written from left to right. The equilibrium constant K_{p_j} is based on partial pressures, and ΔF_j is the free energy change of reaction j. $\Delta F_j|_{298.16}$ is defined as:

$$\Delta F_j \Big|_{298.16} = \Delta H_j \Big|_{298.16} - 298.16\, \Delta S_j \Big|_{298.16}$$

where $\Delta S_j|_{298.16}$ is the standard entropy change for reaction j given by:

$$\Delta S_j \Big|_{298.16} = \sum_{i=1}^{8} a_{ij} S_i + \sum_{i=1}^{5} a_{s_{ij}} S_{s_i} .$$

The S_i's and the S_{s_i}'s are the standard entropies of formation of the species involved (cal/g•mole•K).

The values of most of the required heat capacity coefficients, enthalpies, and entropies are available from many sources. Those currently in use can be found in Ref. 7. Appropriate values for char, on the other hand, are more difficult to obtain. We have adopted the following specification of char properties which relates these thermodynamic properties to char composition:

$$S_{s_2} \Big|_{298.16} = 1.359 + 3.17\bar{a} ,$$

$$h_{F_2} = \begin{cases} 0 & \bar{a} = 0 \\ 2.6 - 68.06 & \bar{a} > 0 \end{cases} ,$$

and

$$C_{s_2} = [\overline{C}_s \text{ (graphite)} + 0.88\bar{a} + 5.8\bar{b}]\, M_2 .$$

Here a and b are stoichiometric coefficients defined previously and $\overline{C}_s$ (graphite) is the heat capacity of graphite on a molar basis (cal/g-mole•K). A brief discussion of the development of these relations is given in App. D.

METHOD OF SOLUTION

The system of equations given by Eqs. 4-9 are solved using finite difference methods. The system of equations has been divided into three sets. One set is a system of first-order ODE's describing gas-phase temperature, velocity, and concentrations. These are ODE's as a result of the quasi-steady state assumption. The second set are those equations describing the solid temperature and densities. These are, in general, partial differential equations. The third set consists of the momentum-balance equations, which, for the current system, have been reduced to Darcy's Equation relating gas-phase pressure to gas-phase velocity. The system of equations is solved on a grid system that can change during the course of a run in order to track high-gradient regions which occur in the solution. The solution is implemented through the use of a FORTRAN computer code.

A general flow sheet describing the solution procedure is given in Fig. 3. The superscripts refer to the time levels, and the tildes indicate temporary solutions which are iterated to convergence. The solution begins by initializing arrays, subroutines, and various balances. Then the gas-phase ODE's at time zero are solved by stepping through the system from inlet to exhaust. Next, Darcy's Equation is solved for pressure by stepping from the exhaust to the inlet end of system. It is not shown in Fig. 3, but these solutions are iterated, if necessary, to obtain convergence of the pressure profile.

After this initial calculation, the remaining solution consists of alternating solutions of the three sets of equations. Time is incremented to a new level n + 1. Estimates are made of temperatures, densities, and rates at the new time level. These are then used in a tentative solution for solid-temperature and solid-

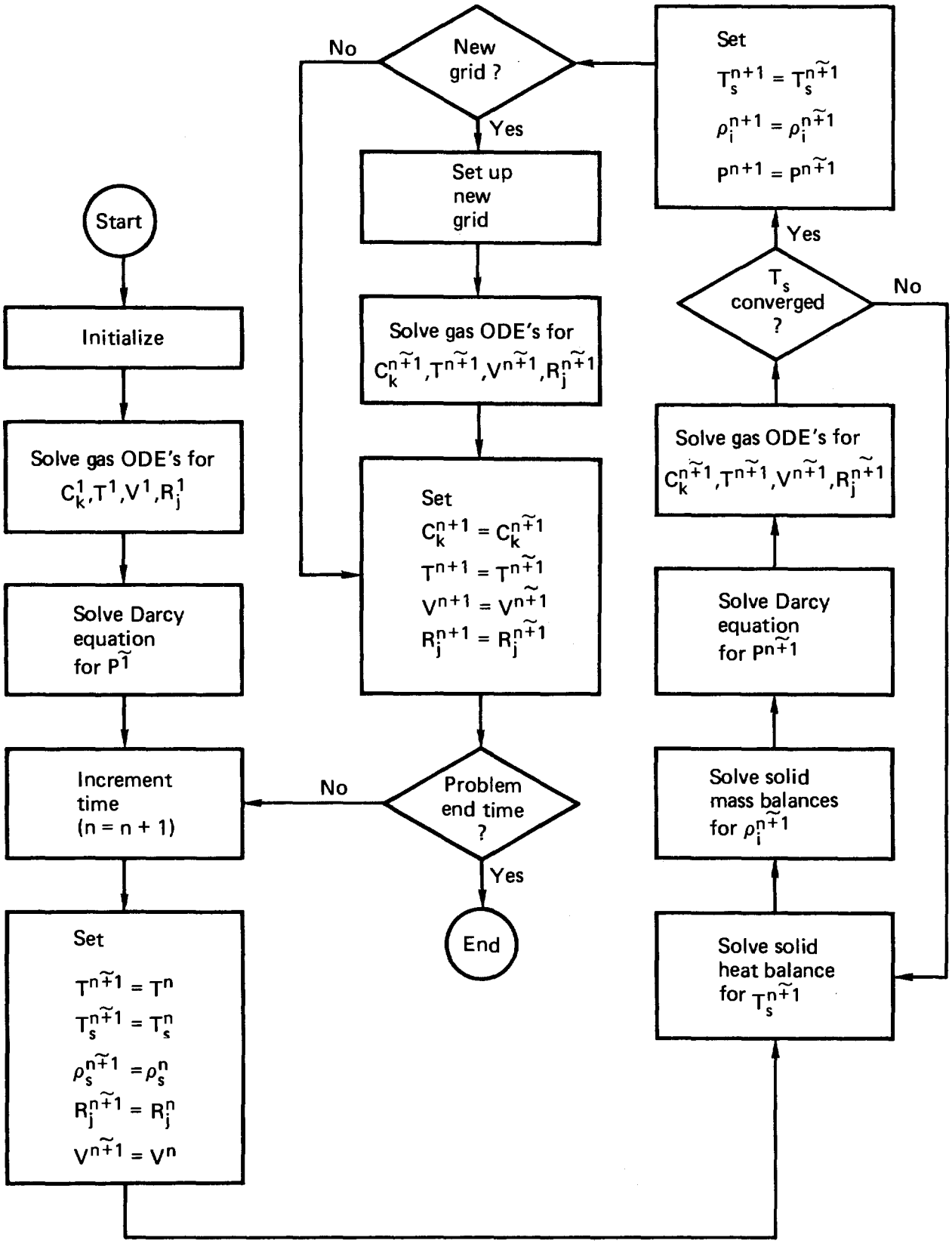

Fig. 3. Logic of the overall solution procedure.

species profiles at the new time level. Using this new state of the system, Darcy's Law is integrated for a new pressure distribution. The gas-phase ODE's are then solved at the new time level and yield new estimates of gas concentrations, temperatures, velocity, and reaction rates at all points of the system. Convergence of the solid-temperature profile is then tested. If the solid-temperature profile has not converged, the newly calculated values of solid temperatures and densities are used in a new solution at the same time level. If the solid-temperature profile has converged, i.e., two successive determinations agree within a prescribed limit, the new values of solid temperatures and densities and the pressure distribution are stored. Testing is then done to determine if the grid system needs to be modified. If no modifications are required, time is incremented and the solution procedure repeated. If the grid system needs to be changed, the changes are made; this is followed by a solution of the gas-phase ODE's over this new grid system. Time is then incremented and solution procedure repeated.

Grid System

The finite-difference grid system used in the problem solution is underlaid by a fixed number of large zones. These major divisions do not change throughout the course of the problem. Each of these large zones can be subdivided into three types of finer zones as the problem progresses in order to track sharp concentrations, temperatures, or pressure gradients. The determination of the necessity of these subdivisions at any point in the system is made by examining reaction rates, pressure gradients, and solid temperature gradients at the point. For details, see App. E.

The three fine subdivisions or zones are designated as type 2, 3, or 4. Those zones left as large zones are type 1. A type 3 subdivision is composed of fine zones, or grid spacings, all of equal size (Δx_s). Type 2 and type 4 subdivisions are a grading from coarse-to-fine and fine-to-coarse zones, respectively. All grid spacings in each type of subdivision are a multiple of Δx_s.

After each rezoning of the problem, values for solid temperature, solid densities, porosity, and pressure are established at any newly created grid points. A linear interpolation between adjacent points is used in the determination.

Gas-Phase ODE's

The gas-phase ODE's consist of a set of ten equations, eight for the gas-phase species, one for the gas-phase temperature, and one for the gas velocity. Any one of a number of standard ODE solution procedures could be used in their solution. Currently, a standard modified Euler scheme is used in the fine zones, and a backward-differencing method is used in the coarse zones for stability reasons. Certain multistep methods could be used to improve accuracy and overcome stability problems, but the uneven grid system makes their application somewhat tedious. The solution of the equations can be carried out in steps from inlet to exhaust since the system of equations only has boundary conditions imposed on the inlet end.

The set of ten equations is obtained from the previously developed Eqs. 4, 6, and 9. The eight species equations solved are:

$$\frac{dC_i}{dx} = \frac{1}{v}\left[-C_i \frac{dv}{dx} + \sum_{j=1}^{11} a_{ij} R_j\right] \tag{22}$$

where $C_i = C_{i_0}$ at $x = 0$.

The temperature equation is:

$$\frac{dT}{dx} = -\frac{1}{V_{c_g}}\left[h_T(T - T_s) + H_g\right] \tag{23}$$

where $T = T_0$ at $x = 0$.

The final equation for the gas-phase velocity is obtained by summing Eq. 22 over all species and replacing the total concentration using the equation of state, Eq. 9. This leads to:

$$\frac{dv}{dx} = -\frac{v}{P}\frac{dP}{dx} + \frac{v}{T}\frac{dT}{dx} + \frac{RT}{P}\left[\sum_{i=1}^{8}\sum_{j=1}^{11} a_{ij} R_j\right] \tag{24}$$

where

$$v = \frac{G}{\sum_{i=1}^{8} C_{i_0}} \quad \text{at } x = 0.$$

Here T_s, P, and dP/dx are treated as known functions of position having been previously tentatively calculated from other equations.

In the coarse zones, a method that is as fully implicit as possible at the new, or downstream, grid location is desirable from a stability standpoint. Stability problems in the numeric solution arise from the following physical circumstance. In many of the coarse zones, the net reaction rate for any of the eleven reactions is low (if it were not, they would have been made into fine zones). However, the low net rate of reaction, especially for reactions 1, 2, and 8, is often a result of a near equilibrium situation. As a consequence of this, one finds that small changes in concentrations, leading the system away from equilibrium, can cause very large changes of rate. This leads to a numerically, but not physically, unstable situation. In more mathematical terms, this is generally described as a stiff system in that it contains characteristic time constants for different changes which differ widely in magnitude. To obtain a more implicit system, one could, in general, introduce the following specification of R_i for the rate at the x_{k+1} grid point, where the solution is known at the x_k location:

$$R_j = R_j\Big|_{\tilde{C}_i(x_{k+1})} + \sum_{i=1}^{8}\left\{\frac{\partial R_j}{\partial C_i}\left[C_i(x_{k+1}) - \tilde{C}_i(x_{k+1})\right]\right\}. \tag{25}$$

Here the tilde represents an estimated value of C_i at the new grid location. This formulation does make the system more fully implicit, but it also requires a matrix inversion to solve for C_i at x_{k+1}.

To overcome the matrix inversion problem, only those terms are retained from Eq. 25 which are felt to be important. Currently, the following set is retained, which has the nice feature that the mass-balance equations can be solved in sequential fashion with no need for a matrix inversion. In the equation for C_3, R_1, and R_2 are replaced by:

$$R_1(x_{k+1}) = R_1\Big|_{\tilde{C}_i(x_{k+1})} + \frac{\partial R_1}{\partial C_3}\left[C_3(x_{k+1}) - \tilde{C}_3(x_{k+1})\right], \tag{26a}$$

$$R_2(x_{k+1}) = R_2\Big|_{\tilde{C}_i(x_{k+1})} + \frac{\partial R_2}{\partial C_3}\left[C_3(x_{k+1}) - \tilde{C}_3(x_{k+1})\right]. \tag{26b}$$

The other rate, R_8, which has the potential to cause a problem, is handled in an approximate fashion by replacing R_8 in the equation for C_6 by:

$$R_8(x_{k+1}) = R_8\Big|_{\tilde{C}_i(x_{k+1})} + \frac{\partial R_8}{\partial C_6}\left[C_6(x_{k+1}) - \tilde{C}_6(x_{k+1})\right]. \tag{27}$$

The set of gas-phase ODE's are solved iteratively across the large grid zones. The following procedure is used to advance from the x_k to the x_{k+1} grid point:

1) Estimate $\tilde{C}_i$, $\tilde{T}$, $\tilde{v}$, and $d\tilde{v}/dx$ at x_{k+1} using the values at x_k and x_{k+1}.
2) Calculate rates and the heat-transfer coefficient at x_{k+1}.

3) Solve Eq. 22 with $i = 6$ for C_6 at x_{k+1}.
4) Recalculate R_8 using Eq. 27.
5) Solve Eq. 22 with $i = 3$ for C_3 at x_{k+1}.
6) Reevaluate R_1 and R_2 using Eq. 26.
7) Solve Eq. 24 for V at x_{k+1}.
8) Solve Eq. 23 for T at x_{k+1}.
9) Check for convergence of concentrations. If the solutions have not converged, use the current values as new estimates of $\tilde{C}_i$, $\tilde{T}$, $\tilde{v}$, and $d\tilde{v}/dx$ at x_{k+1} and repeat from step 2 above.

Rates R_1, R_2, and R_8 are reevaluated to retain consistency in the rates used in all species balances. Currently, step 8 above is omitted except for the first and last iterations, since most R_i's are not a function of T.

Solid-Phase Equations

The solid-phase equations include five mass-balance equations and one energy equation. The solution of the solid heat-balance equation for T_s and mass-balance equation for mobile water, ρ_3, involve space, as well as time derivatives, and are solved with implicit representation of space derivatives at the new time level. The other mass-balance equations contain only time derivatives, and these are thus solved independently at each point in the space dimension.

The solid-temperature equation, Eq. 5, when written in finite difference form at a new time level (see App. F), yields a tridiagonal matrix of coefficients. The solution is obtained using a direct inversion algorithm. For stability reasons related to the strong temperature dependence of evaporation and condensation rates, the source terms in the equation are modified to make them more implicit in solid temperature. The rate terms R_1 and R_2, which are used in obtaining H_s for a solution at the n+1 time level, are modified and become:

$$R_1^{n+1} = \widetilde{R_1^{n+1}} + \frac{\partial R_1}{\partial T_s} (T_s^{n+1} - \widetilde{T_s^{n+1}}),$$

$$R_2^{n+1} = \widetilde{R_2^{n+1}} + \frac{\partial R_1}{\partial T_s} (T_s^{n+1} - \widetilde{T_s^{n+1}}).$$

Note that when $\widetilde{T_s^{n+1}} = T_s^{n+1}$, the correction terms drop out. Other details of the solid-temperature solution procedure are given in App. F.

Equation 8 is solved for ρ_3 using a direct method again to invert the system of equations produced when it is written implicitly at the new time level. The velocity, v_s, required in this solution would, in general, be obtained from some hydrodynamic description of the multiphase water flow problem. However, due to a lack of description of this phenomenon in in situ coal processing, it has been arbitrarily assumed that the water moves at some constant characteristic velocity. This characteristic velocity is currently fixed at one-half the exhaust gas-phase velocity. This simplification undoubtedly fails to adequately model the true liquid water distribution in the system. However, in most cases, this is not a critical consideration in highly permeable media. The main problem from the standpoint of numerical modeling is a means of removing liquid water from the system so that its concentration does not build to unacceptable levels. This assumption is an effective means of accomplishing this task.

The other solid-species balances require only a simple one-step integration in time. The reaction rates used here, as in the T_s and ρ_3 solutions, are just those previously calculated and stored in the solution of the gas-phase ODE's.

Hydrodynamic Equation

The solution of the hydrodynamic equation, Eq. 10, is solved for the gas-phase pressure by a Simpson's Rule integration. The integration proceeds from the exhaust end of the system where the pressure

is known to the inlet end, using previously calculated values of v. The viscosity is determined from the gas-phase temperature and the permeability is calculated as a function of the state of the solid system at each point of space.

SAMPLE CALCULATIONS

Numerous problems were run using the code during its development. The following is a sample of the runs made with the code in its current form. The runs consisted of a simulation of a laboratory experiment, a series of runs at different oxygen-feed levels, and a run with a length scale comparable to those that might occur in a field-scale system. A primary purpose of these three runs was to indicate the type of results that could be obtained from the model. In addition, these runs could be viewed as a partial verification of the numerical model. Qualitatively, they indicate the model is performing adequately. A quantitative judgment is difficult due to a lack of detailed experimental data, the complexity of the system, and the limited number of simulation runs, although the first example below does indicate some degree of quantitative agreement between experimental and calculative results. Some additional verification runs on simplified systems related to the gasification process are reported in App. G.

Experimental Reactor Run

This calculation represents a simulation of some preliminary experimental runs on a 1.5 m long, 0.15 m diameter reactor carried out at this Laboratory. The reactor was packed with approximately 19 kg of crushed coal sized to have a particle diameter of 1 cm. The coal ws gasified with an approximate 6 to 1 steam-to-oxygen feed at an average pressure of about 4.8 atm. Table 2 gives the important input data for the run.

The amount of computed results is quite extensive; however, only selected results illustrating various features of the simulation are given here. Figures 4 (a-c) represent the calculated evolution of the temperature distribution. They show the three fronts associated with the movement of the gasification

Table 2. Input data for reactor simulation.

Parameter	Value
Length	150 cm
Permeability	150 D
Porosity	0.5
$T(x = 0)$	450 K
$T_s(t = 0)$	300 K
$P(x = L)$	4.83 atm
Gas Injection	2×10^{-4} (g-mole)/(cm$^2 \cdot$ s)
Injected Gas Composition	
Mole Fraction O_2	0.134
Mole Fraction H_2O	0.844
Mole Fraction N_2	0.022
Coal Weight Fraction H_2O	0.3
Coal Weight Fraction Ash	0.07
Particle Size	1 cm

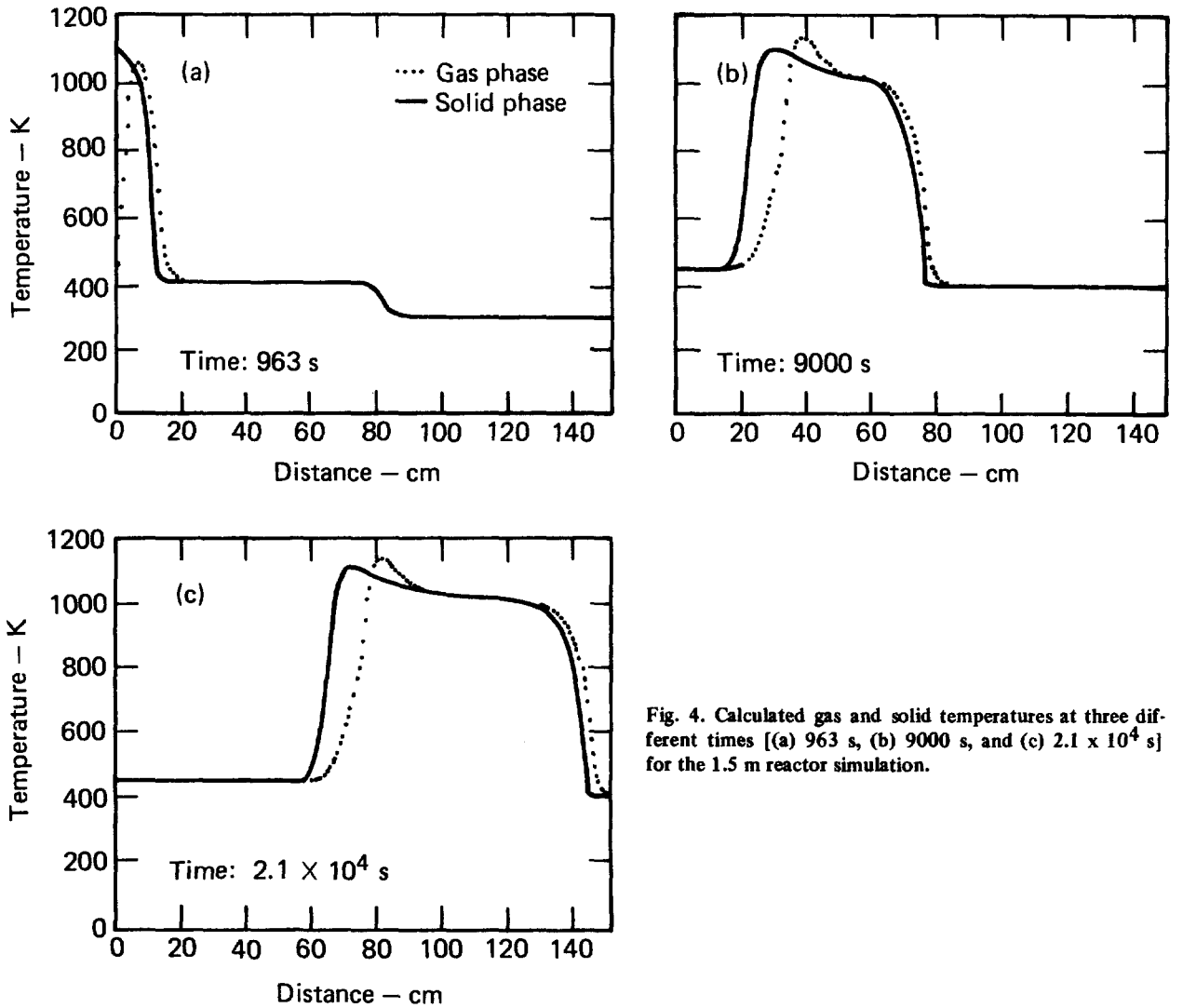

Fig. 4. Calculated gas and solid temperatures at three different times [(a) 963 s, (b) 9000 s, and (c) 2.1 x 10^4 s] for the 1.5 m reactor simulation.

processes through the bed. A condensation front, where considerable steam condensation occurs, is followed by the drying-pyrolysis front, where wet coal is first dried and then pyrolyzed. The third front, the reaction front, represents the point where moving reactants first contact unconsumed char. Note that the growth of the hot char zone as time progresses indicates that the reaction and drying fronts are moving at different velocities. Finally, one sees that in a system of relatively small particles, there are some differences in gas- and solid-phase temperatures, but they are rather limited in extent.

Figure 5 shows the calculated reaction rates as a function of position in the bed after 14,000 seconds of operation. The highest rates are those of pyrolysis and drying. These higher rates are understandable, since they are riding on a sharp temperature gradient. Note the double peak in the water-gas shift reaction, R_8, which is caused by changes in equilibrium limits as the temperature changes.

Figures 6 and 7 represent calculated gas concentration and density profiles after 14,000 seconds of reaction. The initial rapid change (followed by a more gradual one) at the initial contact of gas and char in the hot char zone is evident. The sharp change at $x \cong 115$ cm in due to the drying-pyrolysis front. The small amount of char left unconsumed is a result primarily of neglecting bed settling.

Experimental and calculated results are compared in Figs. 8-11. The experimental data are for two separate runs which differed only in that run 4 was performed with no back heating of the reactor and run 5 had a moderate amount of back heating. The back heating was an attempt to make the performance of the reactor conform to that of a system which did not experience radial heat losses. Gas composition on a dry basis is shown in Fig. 8. The points represent an average value measured in the experiments. The

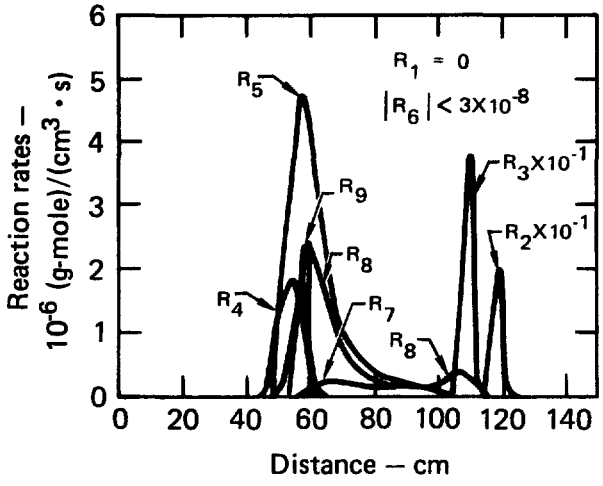

Fig. 5. Calculated reaction rates at time = 1.4 x 10^4 s for the 1.5 m reactor simulation. Reaction rates R_1 and R_6 are omitted since their values are very small.

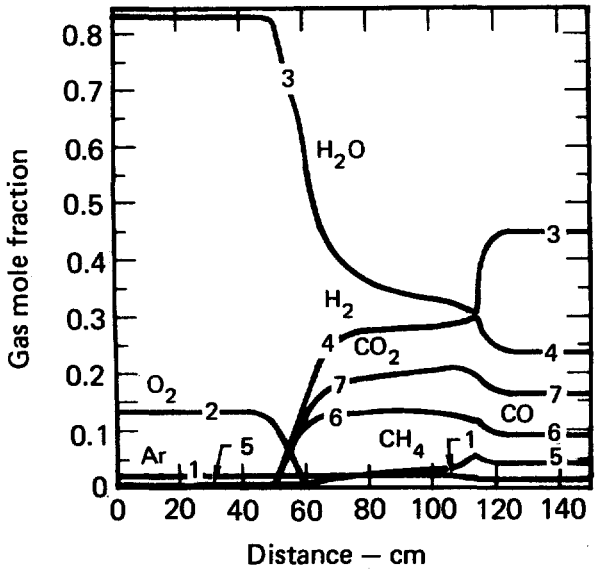

Fig. 6. Calculated gas-phase concentrations at time = 1.4 x 10^4 s for the 1.5 m reactor simulation.

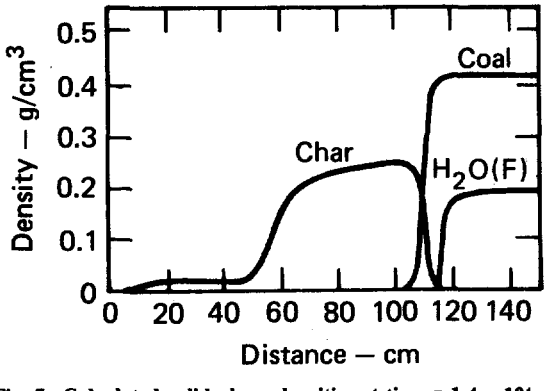

Fig. 7. Calculated solid-phase densities at time = 1.4 x 10^4 s for the 1.5 m reactor simulation.

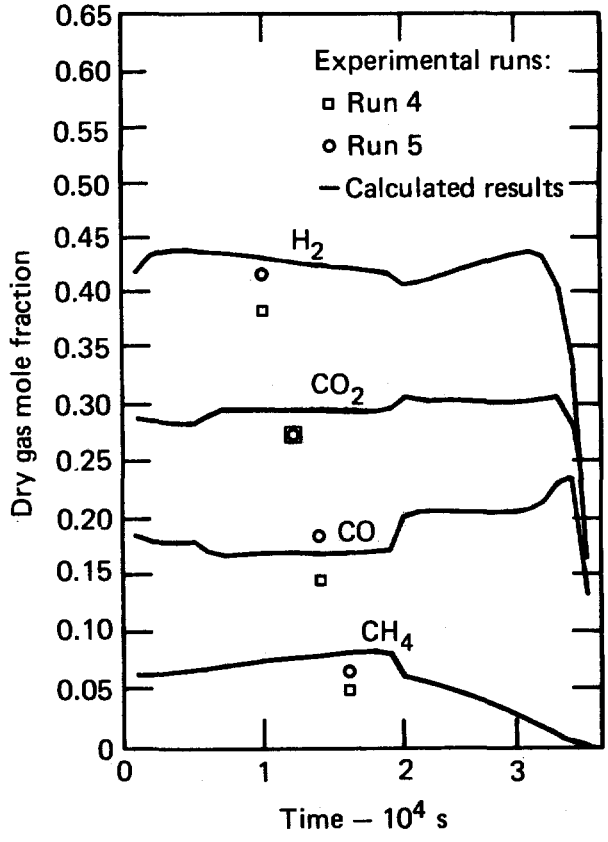

Fig. 8. Calculated exhaust gas composition for the 1.5 m reactor simulation compared to the average gas compositions obtained from two experimental runs.

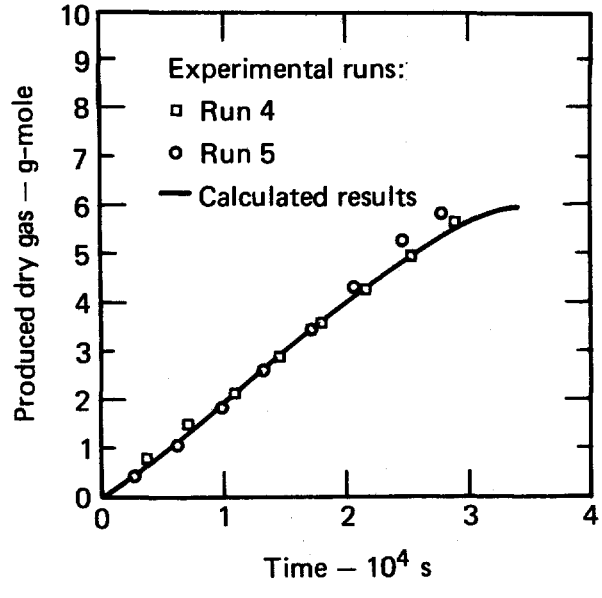

Fig. 9. Calculated production of dry gas for the 1.5 m reactor simulation compared to the production obtained from two experimental runs.

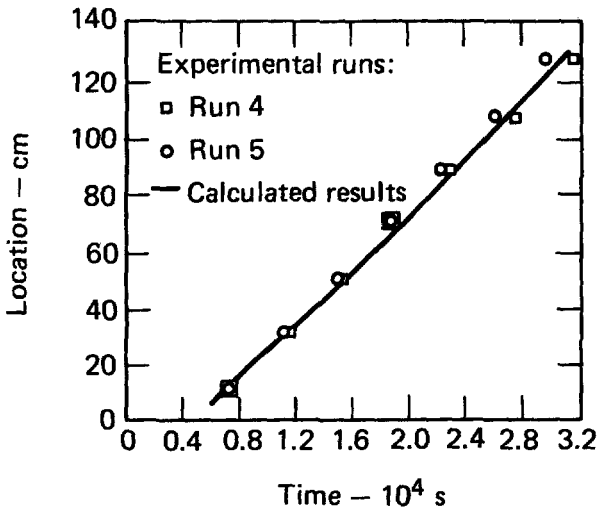

Fig. 10. Calculated reaction front movement for the 1.5 m reactor simulation compared to that obtained from two experimental runs.

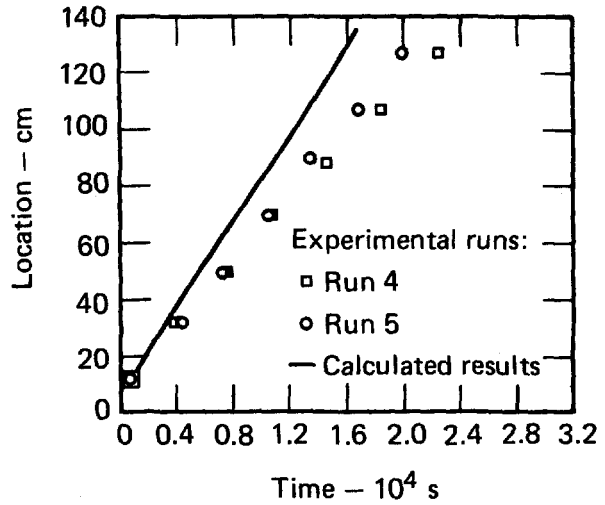

Fig. 11. Calculated drying front movement for the 1.5 m reactor simulation compared to that obtained from two experimental runs.

agreement is rather good, although the experimental results were such that any character in the concentration levels as a function of time was not apparent. Effluent dry gas rates are compared in Fig. 9 and again reasonably good agreement is obtained.

A final comparison of experimental and calculated results is made by comparing positions for the reaction and drying fronts. Figure 10 compares the reaction front positions. The agreement is quite good. This was expected since the rate of front movement is dictated primarily by the rate of coal removal, and calculated and experimental gas compositions were shown to agree quite well. (See Fig. 8.) Figure 11 shows the calculated and experimentally measured location of the drying front. Here we see that the predicted rate of movement is higher than that found experimentally. Unlike the reaction front, the rate of movement of the drying front is quite sensitive to the exact product gas mix, since this mix determines the heat release which in turn is the mechanism driving the front. Additionally, the experimental results indicate there are heat losses occurring in the system that would have their most marked effect on the rate of movement of the drying front.

Beyond the comparison with experimental results, there are several internal checks made by the program that can be used to indicate the model's performance. These include overall balances around the complete system and a consistency check involving the equation of state. Overall carbon balances indicate an error in this run of less than 0.6% of the carbon originally in place. A hydrogen balance shows only 0.1% error in accounting for all the hydrogen entering and leaving the system. Finally, the consistency between ΣCi and the gas equation of state at each point in the system is not directly forced by the solution method. However, in this sample problem, as in the others, the difference between these two values was generally less than 0.1%.

Three Oxygen-Feeds

The system simulated in this series of runs is exactly that described above except that the mole fraction of O_2 in the feed was varied from 0.15 to 0.3, the N_2 mole fraction was set at 0.001, and the outlet pressure was held at 3 atm. The remainder of the feed in each case was steam.

Figures 12 and 13 show the solid and gas temperature distributions for the three runs at a single point in time. As expected, the temperature increased with increased oxygen-feed. also note that the size of the hot char zone is longer for the lower oxygen-feed. This indicates that the relative motion of the drying and reaction fronts is a function of oxygen feed. This is also seen by examining Figs. 14 and 15. The rate of reaction front movement, but not the rate of drying front movement, increases linearly with oxygen feed.

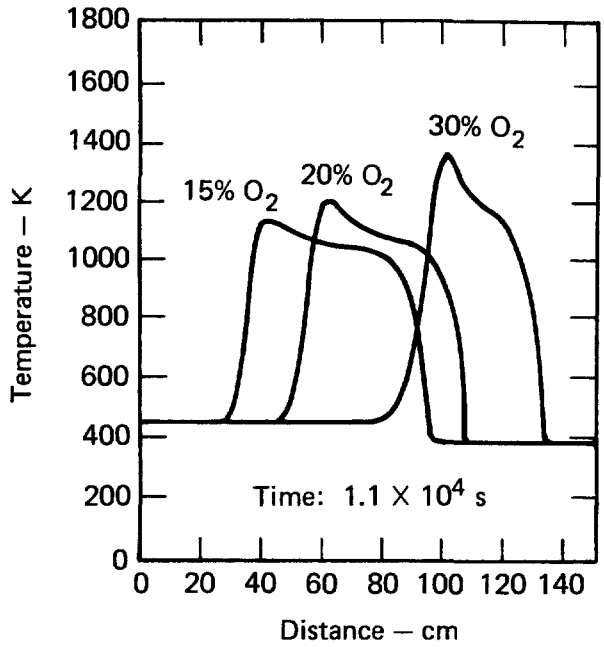

Fig. 12. Calculated solid temperatures at time = 1.1 x 10^4 s for three levels of oxygen-feed concentration.

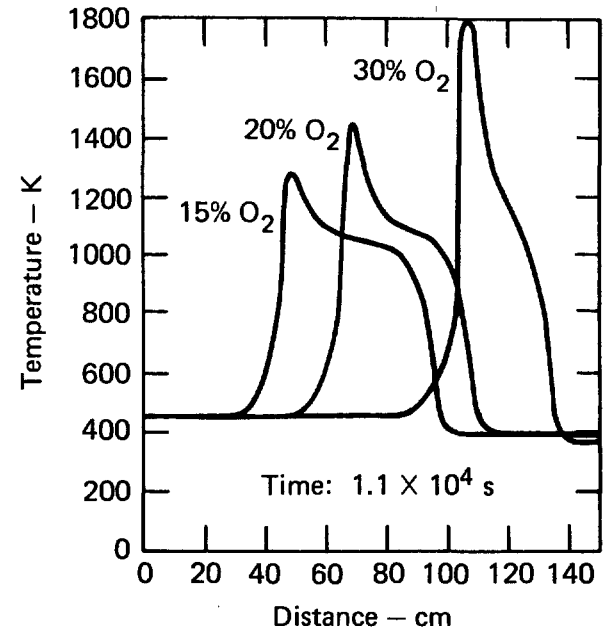

Fig. 13. Calculated gas temperatures at time = 1.1 x 10^4 s for three levels of oxygen-feed concentration.

The relative amounts of the product gases are shown in Figs. 16 and 17. They indicate an increased ratio of CO to CO_2, resulting from the increased temperature generated in the sytem. The total dry gas produced increased at higher oxygen feeds, which is consistent with the higher CO/CO_2 calculated.

As an overall indication of calculated performance, the energy recovery in the gas is shown in Fig. 18. The gas energy is calculated using the heat of combustion of the produced gas at 298 K. The tar heat of combustion is excluded from this calculation. The fractional energy from the original coal is increased slightly at the higher oxygen-feeds and exhibits no maximum over this range of feed. However, the energy recovery per mole of O_2 does have a maximum which indicates an optimum in terms of oxygen consumption at a mole fraction of approximately 0.2.

Field Scale Run

This example was run using the same gas feed as in the experimental reactor run. It differs from that run in that the length is 15 m, the initial porosity is 0.05, the permeability is 20 D, the outlet pressure is 1 atm, and the initial particle size is 20 cm. These conditions were chosen to represent a possible field-scale system.

The developing temperature profile, Fig. 19 (a-b), is similar to that of Fig. 4 (a-b). However, the thermal fronts, particularly the steam front, are more diffuse due to reduced mass transport. Also note that the steam-wet coal region, the zone between $x = 500$ and $x = 1500$ cm at $t = 1 \times 10^5$ s, is not at a constant temperature as it was in the above runs. This is due to the longer pressure gradient in this system, which influences the saturation temperature of the flowing gas stream.

The calculated gas species production is shown in Fig. 20. The total time scale shown represents approximate consumption of one-third of the coal. Also shown on the plot are the calculated results for the 1.5 m reactor simulation. This comparison indicates that trends established prior to arrival of the drying-pyrolysis front at the exhaust end of the shorter system continue to evolve in the longer system. This results in a different compositional mix of produced gas, particularly with regard to methane. This increase in methane is due to the developing of the more extended hot char zone, leading to a more extended reaction region (see Fig. 21).

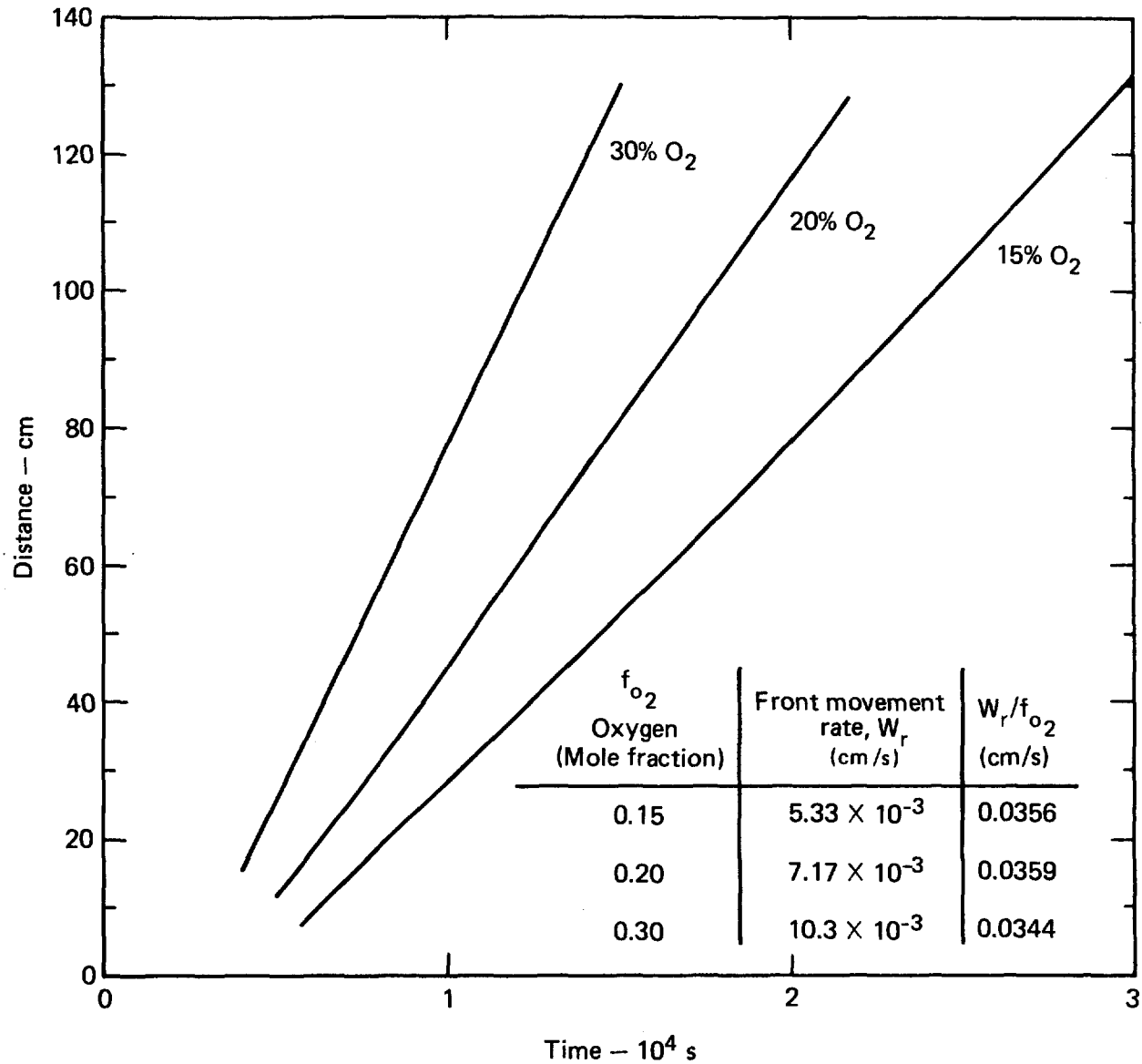

f_{O_2} Oxygen (Mole fraction)	Front movement rate, W_r (cm/s)	W_r/f_{O_2} (cm/s)
0.15	5.33×10^{-3}	0.0356
0.20	7.17×10^{-3}	0.0359
0.30	10.3×10^{-3}	0.0344

Fig. 14. Calculated reaction front movement for three levels of oxygen-feed concentration.

Finally, Figs. 22 and 23 indicate the fashion in which the pressure distribution in a field-scale system might evolve. The injection pressure initially increases due to an increase in resistance in the system, resulting from the growth of a steam zone. It reaches a maximum relatively early and begins a gradual decline. This latter behavior is due to the increase in permeability of the system from char consumption and drying, and pyrolysis of the wet coal. The pressure profiles, Fig. 23, show how the flow resistance is confined to the exhaust end of the system where the undried coal is located.

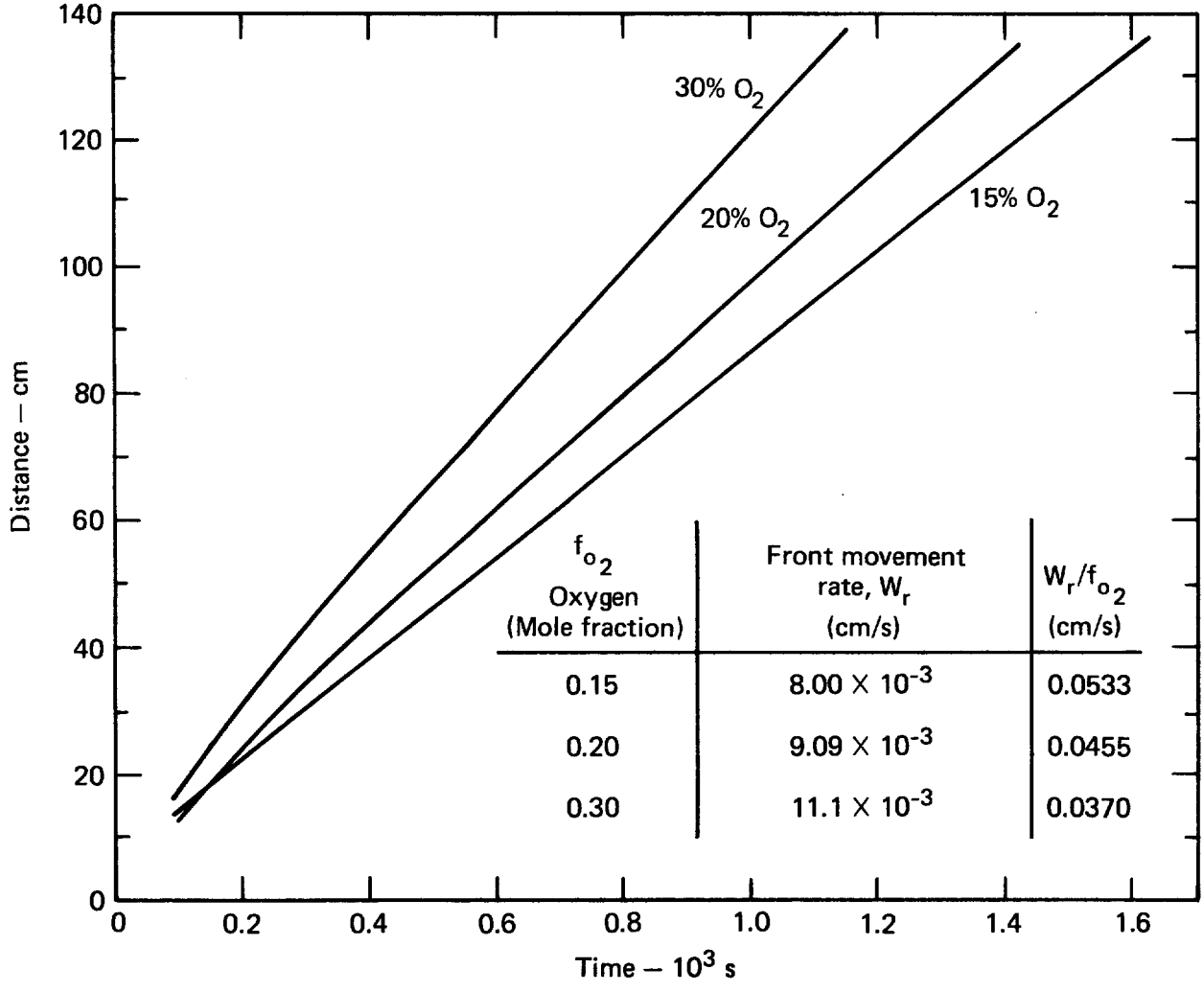

f_{O_2} Oxygen (Mole fraction)	Front movement rate, W_r (cm/s)	W_r/f_{O_2} (cm/s)
0.15	8.00×10^{-3}	0.0533
0.20	9.09×10^{-3}	0.0455
0.30	11.1×10^{-3}	0.0370

Fig. 15. Calculated drying front movement for three levels of oxygen-feed concentration.

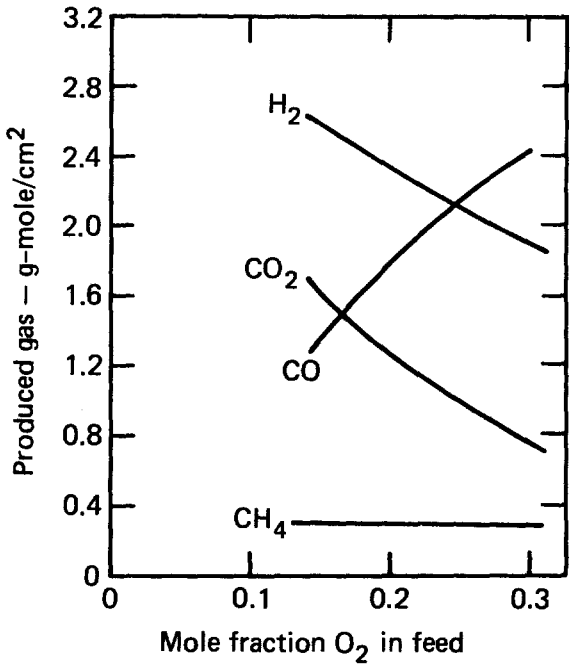

Fig. 16. Calculated production of gas components as a function of oxygen-feed concentration (ϕ = 0.5, P = 3 atm, and L = 150 cm).

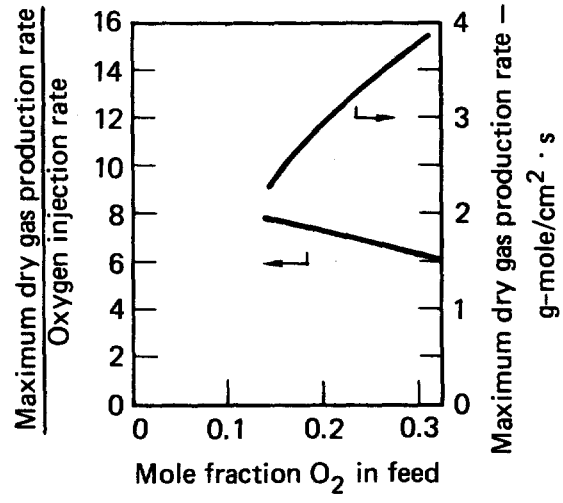

Fig. 17. Calculated production gas flow rate for three levels of oxygen-feed concentration.

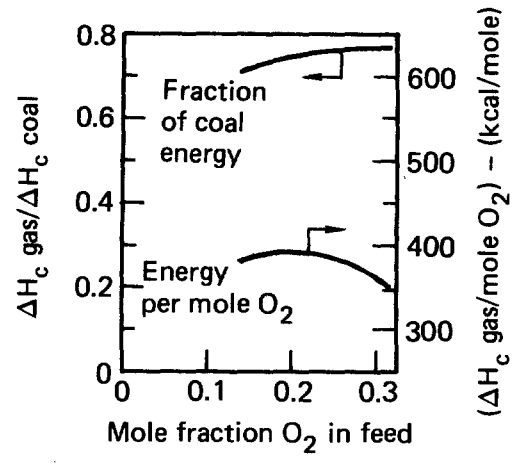

Fig. 18. Calculated energy recovery for three levels of oxygen-feed concentration.

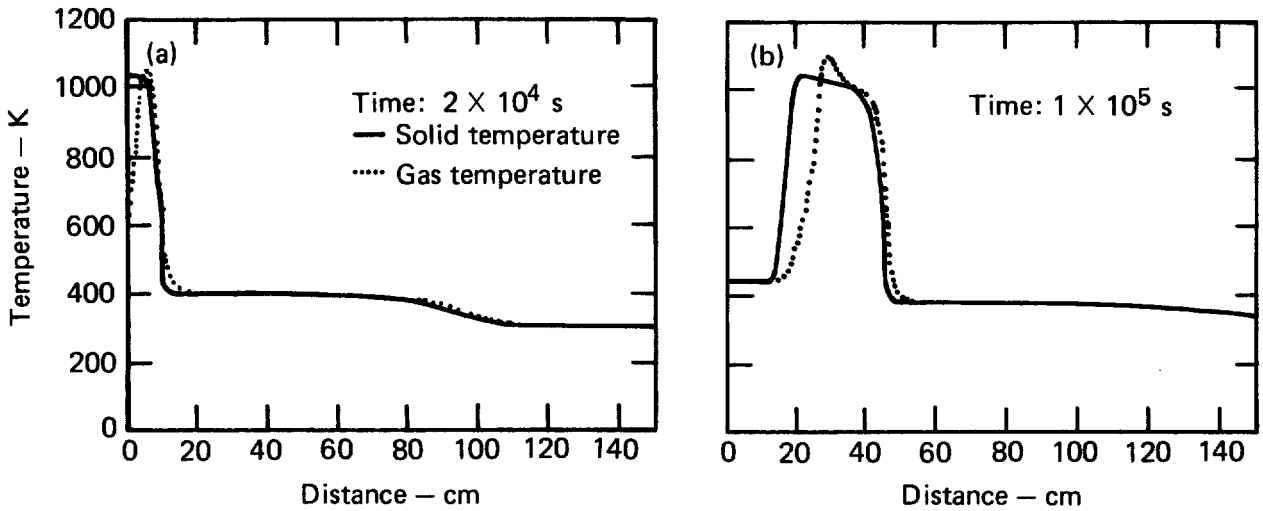

Fig. 19. Calculated gas and solid temperature profiles for the 15 m simulation at a) 2 x 10^4 s and b) 1 x 10^5 s.

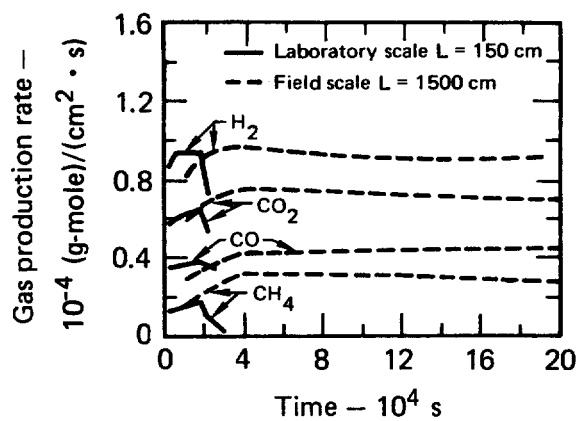

Fig. 20. A comparison of calculated gas production rates for a laboratory and field-scale simulation.

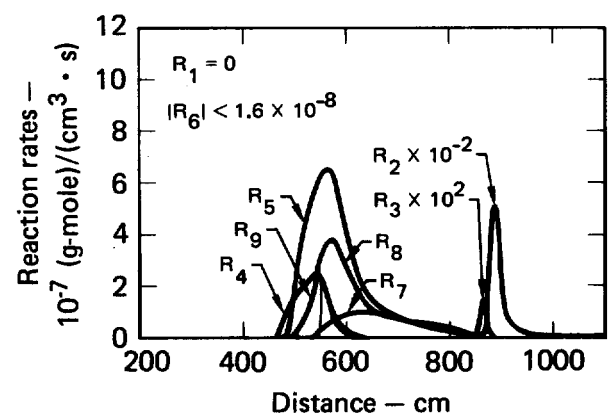

Fig. 21. Calculated reaction rates at time = 2 x 10^5 s for the 15 m simulation. Reaction rates R_1 and R_6 are omitted since their values are very small.

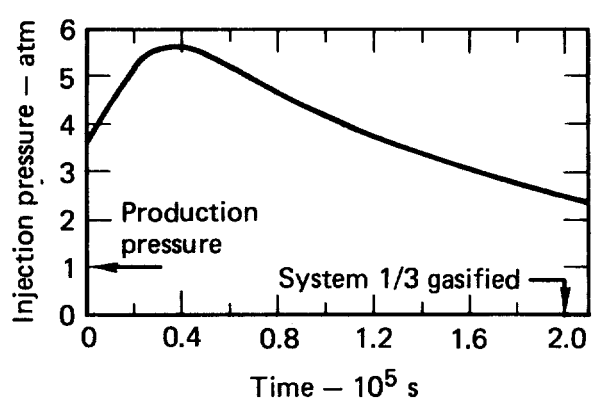

Fig. 22. Calculated injection pressure history for a constant feed rate [2 x 10^{-4} (g-mole)/(cm^2·s)] and production pressure (1 atm) for the field-scale simulation.

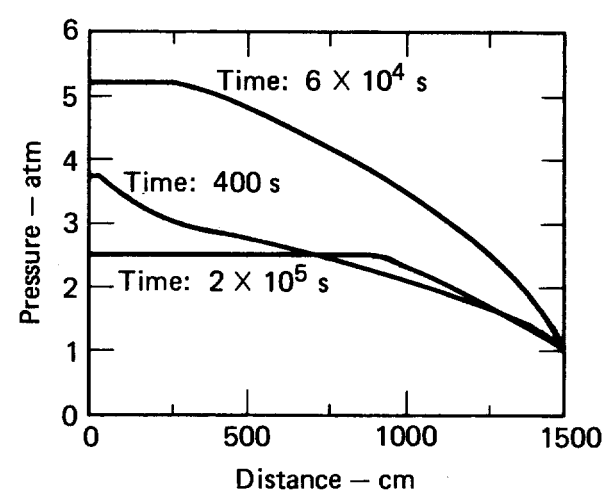

Fig. 23. Calculated pressure profiles at three different times for the field-scale simulation.

NOMENCLATURE

Variable	Description	Units
A	Ratio of bed surface area to bed volume	$\frac{1}{cm}$
a_{ij}	Stoichiometric coefficient of gas species i in reaction j	
$a_{s_{ij}}$	Stoichiometric coefficient of solid species i in reaction j	
c_g	Total gas-phase heat capacity	$\frac{cal}{K \cdot cm^3}$
C_i	Gas concentration of species i	$\frac{mole}{cm^3}$
C_{i_0}	Gas concentration at bed inlet	$\frac{mole}{cm^3}$
$\overline{c_p}$	Average gas molar heat capacity	$\frac{cal}{mole \cdot K}$
c_{p_i}	Molar heat capacity of gas species i	$\frac{cal}{mole \cdot K}$
c_s	Total solid-phase heat capacity	$\frac{cal}{K \cdot cm^3}$
c_{s_i}	Heat capacity of solid species i	$\frac{cal}{g \cdot K}$
C_T	Total gas concentration	$\frac{mole}{cm^3}$
d	Particle diameter	cm
f_j	Heat-splitting parameter for reaction j	
G	Molar gas-injection rate	$\frac{mole}{s \cdot cm^2}$
h_{f_i}	Standard heat of formation of species i	$\frac{cal}{mole}$
H_g	Gas-phase heat source	$\frac{cal}{s \cdot cm^3}$
h_i	Molar enthalpy of gas species i	$\frac{cal}{mole}$
H_s	Solid-phase heat source	$\frac{cal}{s \cdot cm^3}$
h_{s_i}	Molar enthalpy of solid species i	$\frac{cal}{mole}$
h_T	Heat-transfer coefficient	$\frac{cal}{s \cdot K \cdot cm^3}$
K	Permeability	cm^2
k	Effective thermal conductivity	$\frac{cal}{s \cdot K \cdot cm}$
K_{E_j}	Equilibrium constant associated with reaction j	

Variable	Description	Units
k_y	Mass-transfer coefficient	$\frac{mole}{s \cdot cm^3}$
L	System length	cm
M_i	Molecular weight of solid species i	
P	Pressure	atm
P	Vapor pressure of water	atm
Pr	Prandtl number	
R	Gas constant	$\frac{cm^3 \cdot atm}{mole \cdot K}$
R_{c_j}	Effective chemical rate of reaction j	$\frac{mole}{s \cdot cm^3}$
Re	Reynolds number	
R_j	Rate of reaction j	$\frac{mole}{s \cdot cm^3}$
R_{m_j}	Mass-transfer rate associated with reaction j	$\frac{mole}{s \cdot cm^3}$
S	Shape factor	
Sc	Schmidt number	
S_i	Entropy of gas species i	$\frac{cal}{mole \cdot K}$
S_{s_i}	Entropy of solid species i	$\frac{cal}{mole \cdot K}$
T	Gas-phase temperature	K
t	Time	s
T_0	Inlet gas temperature	K
T_s	Solid-phase temperature	K
T_{s_0}	Initial temperature of bed	K
v	Superficial gas velocity	$\frac{cm}{s}$
V_{s_i}	Velocity of solid species i	$\frac{cm}{s}$
x	Space dimension	cm
y_i	Gas mole fraction of species i	
ΔF_j	Free energy change for reaction j	$\frac{cal}{mole}$
ΔH_j	Heat effect of reaction j	$\frac{cal}{mole}$

Variable	Description	Units
ΔS_j	Entropy change for reaction j	$\frac{cal}{mole \cdot K}$
λ_g	Gas thermal conductivity	$\frac{cal}{s \cdot K \cdot cm}$
λ_s	Solid thermal conductivity	$\frac{cal}{s \cdot K \cdot cm}$
μ	Viscosity	cps
ν	Kinematic viscosity	$\frac{cm^2}{s}$
ρ_i	Density of solid species i	$\frac{g}{cm^3}$
ρ_{i_0}	Initial density of solid species i	$\frac{g}{cm^3}$
ϕ	Porosity	
α	Permeability parameter	

Solids

subscripts	1	Coal (daf)
	2	Char
	3	"Mobile" water
	4	"Fixed" water
	5	Ash

Gases

subscripts	1	N_2 (or inert gas)
	2	O_2
	3	H_2O
	4	H_2
	5	CH_4
	6	CO
	7	CO_2
	8	Tar

APPENDIX A
COAL PERMEABILITY CORRELATION

The pressure drop in a one-dimensional coal bed can be represented by Darcy's law:

$$v = -\frac{K}{\mu}\frac{dP}{dx}$$

where the permeability, K, is a function of porosity, ϕ, as well as species densities, ρ_i. Thus, as gasification proceeds and the porosity increases, the permeability can also be expected to increase.

The simplest pore model of equal-site cylindrical pores, whose radius increases as gasification progresses, is given by the Hagen-Poiseulle law:

$$v_{pore} = -\frac{R^2}{8\mu}\frac{dP}{dx} .$$

Thus, $v = N\pi R^2 v_{pore}$ where N = number of pores per unit area.

For initial radius R_0 and porosity ϕ_0,

$$\frac{\phi}{\phi_0} = \left(\frac{R}{R_0}\right)^2$$

and

$$K = -\frac{v\mu}{dP/dx} = \frac{N\pi R^4}{8} = \frac{R^2\phi}{8} = \frac{R_0{}^2\phi^2}{8\phi_0}$$

which is proportional to ϕ^2. However, if data are examined for a change in permeability of Wyodak coal during drying (and pyrolysis),[8] coupled with an estimate of porosity in this coal,[9] this relationship is not found to hold.

The data from Table A-1 are plotted on a log/log basis in Fig. A-1 and as log K versus $\Delta\phi$ in Fig. A-2. It can be seen that K is not proportional to ϕ^2; that is, a parallel capillary model is not justified. This is not surprising because additional fractures are observed to occur as porosity increases. From Fig. A-2 it can be noted that log K is very nearly a linear function of $\Delta\phi$ over the range studied. On this empirical basis, take:

Table A-1. Permeability, weight, and porosity change for Dekker coal as a function of temperature.

Temperature (°C)	Permeability[9] (D)	Fractional weight Loss[8]	Porosity change $\Delta\phi$
30	1×10^{-2}	0.01	0.013
60	2×10^{-2}	0.05	0.065
90	7×10^{-2}	0.15	0.19
120	2×10^{-1}	0.18	0.23
120-300	0.8	0.18-0.21	0.23-0.27
490	1.2	0.35	0.40
550	3.0	0.37	0.42
610	7.0	0.40	0.45
650	16.0	0.45	0.49

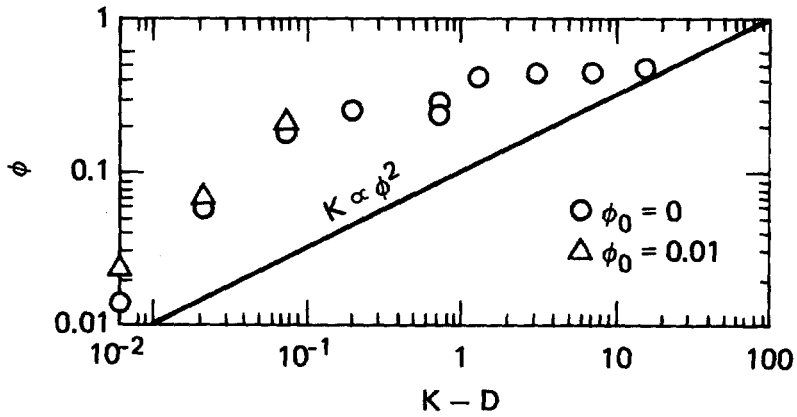

Fig. A-1. Permeability (K) versus porosity (ϕ) for Wyodak coal during drying and pyrolysis.

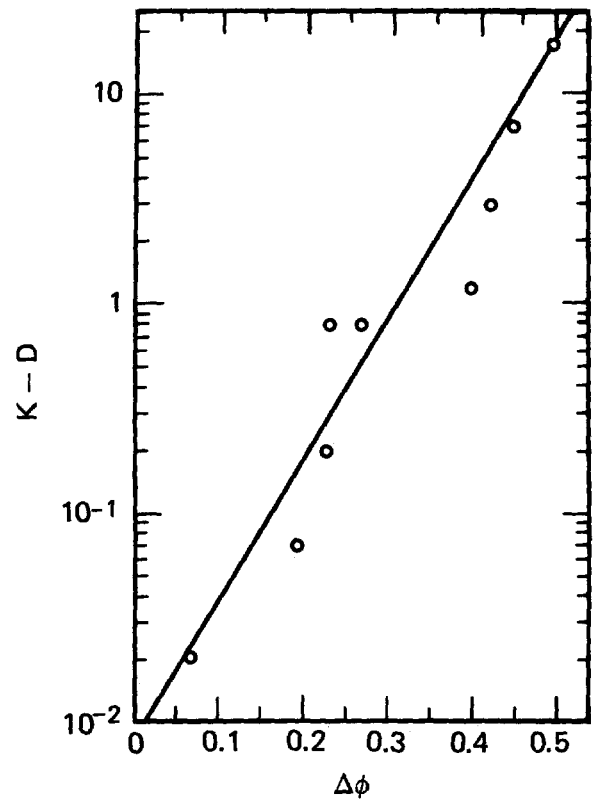

Fig. A-2. Permeability (K) versus the change in porosity (ϕ) for Wyodak coal during drying and pyrolysis.

$$\ln \frac{K}{K_0} = \alpha\,(\phi - \phi_0)$$

or

$$\frac{K}{K_0} = e^{\alpha(\phi - \phi_0)}$$

where α has a value of approximately 12. For Wyodak coal, this relationship must cease to hold as ϕ approaches unity, where K should become very large. Therefore, the above relation is applied only for ϕ less than some value, ϕ_ℓ, at which point the pressure drop is quite small in any event.

APPENDIX B
STOICHIOMETRIC COEFFICIENTS

General Coefficients

The following input information is required to specify all stoichiometric coefficients:

- Coal composition parameters a and b for coal molecule CH_aO_b.
- Char composition parameters $\bar{a}$ and $\bar{b}$ for char molecule $CH_{\bar{a}}O_{\bar{b}}$.
- Moles of char per mole of coal $a_{s_{2,3}}$.
- Atoms of C in coal which become atoms of C in tar s.
- Moles H_2 per mole of coal $a_{4,3}$.
- Moles CH_4 per mole of coal $a_{5,3}$.
- H to C ratio of tar r.

The coefficients for each of the eleven reactions are given below. All other unspecified coefficients are 0. A minus sign denotes removal of a species when the reaction proceeds from left to right as written.

1) $R_1 \quad |a_{s_{3,1}}| H_2O(M) \rightleftharpoons |a_{3,1}| H_2O(g)$

$$a_{s_{3,1}} = -1 \quad a_{3,1} = 1$$

2) $R_2 \quad |a_{s_{4,2}}| H_2O(F) \rightarrow |a_{3,2}| H_2O(g)$

$$a_{s_{4,2}} = -1 \quad a_{3,2} = 1$$

3) $R_3 \quad |a_{s_{1,3}}| CH_aO_b \rightarrow |a_{s_{2,3}}| CH_{\bar{a}}O_{\bar{b}} + |a_{3,3}| H_2O + |a_{4,3}| H_2 + |a_{5,3}| CH_4$

$$+ |a_{6,3}| CO + |a_{7,3}| CO_2 + |a_{8,3}| C_9H_c$$

Note that it has been arbitrarily assumed that tar contains 9 carbons.

$a_{s_{1,3}} = -1$ $\qquad a_{3,3} = \frac{1}{2}\,[a - \bar{a}a_{10,3} - 2a_{4,3} - 4a_{5,3} - rs]$

$a_{s_{2,3}}$ = input value $\qquad a_{6,3} = 1 - a_{s_{2,3}} - a_{7,3} - a_{5,3} - s$

$a_{4,3}$ = input value $\qquad a_{7,3} = b - 1 + a_{s_{2,3}}(1 - \bar{b}) - a_{3,3} + a_{5,3} + s$

$a_{5,3}$ = input value $\qquad a_{8,3} = \frac{s}{9}$

4) $R_4 \quad |a_{s_{2,4}}| CH_{\bar{a}}O_{\bar{b}} + |a_{2,4}| O_2 \rightarrow |a_{7,4}| CO_2 + |a_{3,4}| H_2O$

$a_{s_{2,4}} = -1$ $\qquad a_{3,4} = \frac{\bar{a}}{2}$

$a_{2,4} = -(1 + \frac{\bar{a}}{4} - \frac{\bar{b}}{2})$ $\qquad a_{7,4} = 1$

5) R_5 $|a_{s_{2,5}}|\ CH_{\bar{a}}O_{\bar{b}} + |a_{3,5}|\ H_2O \rightleftharpoons |a_{6,5}|\ CO + |a_{4,5}|\ H_2$

$a_{s_{2,5}} = -1 \qquad a_{4,5} = 1 + \frac{\bar{a}}{2} - \bar{b}$

$a_{3,5} = -1 + \bar{b} \qquad a_{6,5} = 1$

6) R_6 $|a_{s_{2,6}}|\ CH_{\bar{a}}O_{\bar{b}} + |a_{7,6}|\ CO_2 \rightleftharpoons |a_{6,6}|\ CO + |a_{3,6}|\ H_2O$

$a_{s_{2,6}} = -1 \qquad a_{6,6} = 2 + \frac{\bar{a}}{2} - \bar{b}$

$a_{3,6} = \frac{\bar{a}}{2} \qquad a_{7,6} = -1 - \frac{\bar{a}}{2} + \bar{b}$

7) R_7 $|a_{s_{2,7}}|\ CH_{\bar{a}}O_{\bar{b}} + |a_{4,7}|\ H_2 \rightleftharpoons |a_{5,7}|\ CH_4 + |a_{6,7}|\ CO$.

$a_{s_{2,7}} = -1 \qquad a_{5,7} = 1 - \bar{b}$

$a_{4,7} = -2(1 - \frac{\bar{a}}{4} - \bar{b}) \qquad a_{6,7} = \bar{b}$

8) R_8 $|a_{6,8}|\ CO + |a_{3,8}|\ H_2O(g) \rightleftharpoons |a_{7,8}|\ CO_2 + |a_{4,8}|\ H_2$

$a_{3,8} = -1 \qquad a_{6,8} = -1$

$a_{4,8} = 1 \qquad a_{7,8} = 1$

9) R_9 $|a_{4,9}|\ H_2 + |a_{2,9}|\ O_2 \rightarrow |a_{3,9}|\ H_2O(g)$

$a_{2,9} = -1 \qquad a_{4,9} = -2$

$a_{3,9} = 2$

10) R_{10} $|a_{6,10}|\ CO + |a_{2,10}|\ O_2 \rightarrow |a_{7,10}|\ CO_2$

$a_{2,10} = -1 \qquad a_{7,10} = 2$

$a_{6,10} = -2$

11) R_{11} $|a_{5,11}|\ CH_4 + |a_{2,11}|\ O_2 \rightarrow |a_{7,11}|\ CO_2 + |a_{3,11}|\ H_2O(g)$

$a_{2,11} = -2 \qquad a_{5,11} = -1$

$a_{3,11} = 2 \qquad a_{7,11} = 1$

Coefficients for Wyodak Coal

The following is a typical set of stoichiometric coefficients calculated for a subbituminous coal from the Wyodak mine in Wyoming. The input data is based on the work of Campbell[10] and Taylor and Bowen.[11]

Input data:

$a = 0.912$	$s = 0.123$
$b = 0.194$	$a_{4,2} = 0.044$
$\bar{a} = 0.090$	$a_{5,3} = 0.083$
$\bar{b} = 0.016$	$r = 2.811$
$a_{s_{2,3}} = 0.766$	

Nonzero coefficients:

$a_{s_{3,1}} = -1$	$a_{3,6} = 0.045$
$a_{3,1} = 1$	$a_{6,6} = 2.029$
$a_{s_{4,2}} = -1$	$a_{7,6} = -1.029$
$a_{3,2} = 1$	$a_{s_{2,7}} = -1$
$a_{s_{1,3}} = -1$	$a_{4,7} = -1.923$
$a_{s_{2,3}} = 0.766$	$a_{5,7} = 0.984$
$a_{3,3} = 0.078$	$a_{6,7} = 0.016$
$a_{4,3} = 0.083$	$a_{3,8} = -1$
$a_{5,3} = 0.044$	$a_{4,8} = 1$
$a_{6,3} = 0.030$	$a_{6,8} = -1$
$a_{7,3} = 0.037$	$a_{7,8} = 1$
$a_{8,3} = 0.014$	$a_{2,9} = -1$
$a_{s_{2,4}} = -1$	$a_{3,9} = 2$
$a_{2,4} = -1.014$	$a_{4,9} = -2$
$a_{3,4} = 0.045$	$a_{2,10} = -1$
$a_{7,4} = 1$	$a_{6,10} = -2$
$a_{s_{2,5}} = -1$	$a_{7,10} = 2$
$a_{3,5} = -0.984$	$a_{2,11} = -2$
$a_{4,5} = 0.045$	$a_{3,11} = 2$
$a_{6,5} = 1$	$a_{5,11} = -1$
$a_{s_{2,6}} = -1$	$a_{7,11} = 1$

APPENDIX C
RATE EQUATIONS

Detailed specifications of reaction rates used in the model are given below.

1. Evaporation/condensation of mobile water.

R_1: $H_2O(M) \leftrightharpoons H_2O(g)$

a) $R_1 = k_y(P/P - y_3)$

where $P = \exp[12.61 - (4690/\tilde{T}_1)]$. We define the reaction temperature of interest $\tilde{T}_1$ as $\tilde{T}_1 = \beta_1 T_s + (1 - \beta_1)T$. Initially β_1 has been set to 1. Also P/P is always less than or equal to 1.

b) A special limiting case for ρ_3 is used to improve the numerical stability

$$R_1 = \frac{0.5\rho_3}{M_3 \Delta t}$$

if

$$2\Delta t \left(k_y \frac{P}{P} - y_3\right) M_3 > \rho_3 .$$

Here Δt is the current numerical time-step size.

2. Coal drying.

R_2: $H_2O(F) \rightarrow H_2O(g)$

This drying is as much controlled by internal diffusion in the coal particles as by the surface mass transfer coefficient. In the manner of Newman,[12] we assumed internal transfer is under a H_2O concentration driving force.

The flux of water is defined as

$$q = -D^* \Delta\rho$$

where ρ is the mass H_2O/unit volume and D^* is the effective diffusivity (1.3×10^{-5} cm^2/s in Dekker coal). At the particle surface,

$$q = +k_y\left(\frac{P}{P}\frac{\rho}{\rho^*} - y_3\right)$$

where ρ^* is the saturated water concentration in particle, y_3 is the H_2O mole fraction in bulk gas, and P is the vapor pressure at T_s.

If a uniform initial liquid concentration ρ_0 is considered, the solution of this system for a spherical, symmetric, coal particle is given, under conditions where a series can be truncated at its first terms ($D^* \ll 1$ and many times greater than d/D^*), by

$$q \simeq k_y\left(\frac{P}{P}\frac{\rho}{\rho^*} - y_3\right)\frac{\gamma^2}{3\eta}$$

where $\eta \equiv (k_y P^d)/(2P\rho^* D^*)$ and γ is the first Eigenvalue given by $\tan \gamma_n = (\gamma_n)/(1 - \eta)$. For $\rho_0 = \rho^*$, for long drying times, this gives:

$$R_2 \simeq k_y \frac{\gamma^3}{3\eta}\left(\frac{P}{P}\frac{\rho}{\rho_0} - y_3\right).$$

For particle temperatures greater than the water-boiling point, that is $P > P$, the drying rate by the mechanism considered above is limited to that occurring at $P = P$ augmented by a heat-transfer controlled term (proportional to $h(T_s - T_B)$ where $P(T_B) = P$). Here

$$R_2 = k_y \frac{\gamma^2}{3\eta}\left(\frac{\rho}{\rho_0} - y_3\right) + \frac{\alpha' h}{\Delta H^v}(T - T_B) = k_y \frac{\gamma^2}{3\eta}\left(\frac{\rho}{\rho_0} - y_3\right) + \alpha k_y (T - T_B).$$

The arbitrary constant α is selected for smooth behavior at $T_s = T_B$, giving $\alpha = E^*/T_B^2$ where $E^* = 4690$ K, the exponential energy term in the vapor pressure relationship.

Limitations are also applied to R_2 to prevent overevaporation of water in one time-step. Basically, if calculated R_2 would cause overevaporation (more than half of remaining water), and R_m would just evaporate all water in next time step, then:

$$R_{2\,(\text{limited})} = R_m * \left(1 - \frac{1}{2}\exp\left[1 - \frac{R_2}{R_m/2}\right]\right).$$

3. Coal pyrolysis.

$$R_3:\ CH_aO_b \rightarrow |a_{s_{2,3}}|\ CH_{\bar{a}}O_{\bar{b}} + |a_{5,3}|\ CH_4$$

$$+ |a_{3,3}|\ H_2O(g) + |a_{6,3}|\ CO + |a_{4,3}|\ H_2 + |a_{7,3}|\ CO_2 + |a_{8,3}|\ C_9H_c$$

The reaction rate was obtained for Wyodak coal, a western subbituminous coal, from data in Ref. 10:

$$R_3 = \frac{5.\,\rho_1 \exp(-6039/T_s)}{M_1}.$$

4. Char oxidation.

$$R_4:\ CH_{\bar{a}}O_{\bar{b}} + |a_{2,4}|\ O_2 \rightarrow CO_2 + |a_{3,4}|\ H_2O(g)$$

a) Base chemical rate from Ref. 13:

$$R^+_{c_4} = \frac{9.55 \times 10^8\ \rho_2\ Py_2 \exp(-22142/\tilde{T}_2)}{M_2\ \tilde{T}_2^{\,1/2}}.$$

We define the reaction temperature of interest $\tilde{T}_2$ as $\tilde{T}_2 = \beta_2 T_s + (1 - \beta_2)T$. Initially β_2 has been set to 1. The rate above has been increased by a factor of 100 over that found in Ref. 13 to account for the higher surface area of char.

b) This reaction is not constrained by equilibrium:

$$R_{c_4} = R^+_{c_4}.$$

c) Overall rate, including mass transfer limitation:

$$R_4 = \frac{1}{\left(1/R_{c_4}\right) + \left(1/k_y y_2\right)}.$$

5. Steam/char reaction.

$$R_5:\ CH_{\bar{a}}O_{\bar{b}} + |a_{3,5}|\ H_2O(g) \rightleftharpoons CO + |a_{4,5}|\ H_2O(g)$$

a) Base chemical rate from Ref. 14:

$$R^{+}_{c_5} = \frac{\rho_2 P^2 y_3^2 \exp\left(5.052 - 12908/\tilde{T}_2\right)}{M_2\left[y_3 P + \exp\left(-22.216 + 24880/\tilde{T}_2\right)\right]^2} .$$

We define the reaction temperature of interest $\tilde{T}_2$ as $\tilde{T}_2 = \beta_2 T_s + (1 - \beta_2)T$. Initially β_2 has been set to 1.

b) Rate, including equilibrium limitation:

$$R_{c_5} = \frac{R^{+}_{c_5}}{y_3}\left(y_3 - \frac{y_6 y_4}{K_{E_5}}\right) .$$

The equilibrium relation assumes $|a_{3,5}| \cong |a_{4,5}| \cong |a_{6,5}| \cong 1$.

c) Overall rate, including mass transfer limitation.

(1) If $y_3 - (y_6 y_4 / K_{E_5}) > 0$ (i.e., forward reaction), then:

$$R_5 = \frac{1}{\left(1/R_{c_5}\right) + \left(1/k_y y_3\right)} .$$

Here we assume $|a_{3,5}| \cong 1$.

(2) If $y_3 - (y_6 y_4 / K_{E_5}) < 0$ (i.e., reverse reaction), then:

$$R_5 = \frac{1}{\left(1/R_{c_5}\right) + \left(1/-k_y y_6\right)} .$$

Here we assume $|a_{6,5}| \cong 1$.

6. CO_2 char reaction.

$$R_6: \quad CH_{\bar{a}}O_{\bar{b}} + |a_{7,6}|\ CO_2 \rightleftharpoons |a_{6,6}|\ CO + |a_{3,6}|\ H_2O(g)$$

a) Base chemical rate from Ref. 15:

$$R^{+}_{c_6} = \frac{1.15 \times 10^4\ \rho_2 P y_7 \exp\left(-23956/\tilde{T}_2\right)}{M_2\left[1. + 0.014\ P y_6\ \exp\left(7549/\tilde{T}_2\right) + 0.21\ P y_7 \exp\left(3171/\tilde{T}_2\right)\right]} .$$

We define the reaction temperature of interest $\tilde{T}_2$ as $\tilde{T}_2 = \beta_2 T_s + (1 - \beta_2)T$. Initially β_2 has been set to 1.

b) Rate, including equilibrium limitation:

$$R_{c_6} = \frac{R^{+}_{c_6}}{y_7}\left(y_7 - \frac{y_6^2}{K_{E_6}}\right).$$

The equilibrium relation assumes $|a_{7,6}| \cong 1$ and $|a_{6,6}| \cong 2$.

c) Overall rate, including mass transfer limitation.

(1) If $y_7 - (y_6^2/K_{E_6}) < 0$ (i.e., forward reaction), then:

$$R_6 = \frac{1}{\left(1/R_{c_6}\right) + \left(1/k_y y_7\right)} .$$

Here we assume $|a_{7,6}| \cong 1$.

(2) If $y_7 - (y_6^2/K_{E_6}) < 0$ (i.e., reverse reaction), then:

$$R_6 = \frac{1}{\left(1/R_{c_6}\right) + \left(2/-k_y y_6\right)} .$$

Here we assume $|a_{6,6}| \cong 2$.

7. Hydrogen char reaction.

R_7: $CH_a^- O_b^- + |a_{4,7}|\ H_2 \rightleftharpoons CH_4 + |a_{6,7}|\ CO$

a) Base chemical rate from Ref. 14:

$$R_{c_7}^+ = \frac{\rho_2 P^2 y_4^2 \exp\left(2.803 - (13673/\tilde{T}_2)\right)}{M_2\left[1 + P y_4 \exp\left(-10.452 + (11698/\tilde{T}_2)\right)\right]} .$$

We define the reaction temperature of interest $\tilde{T}_2$ as $\tilde{T}_2 = \beta_2 T_s + (1 - \beta_2)T$. Initially β_2 has been set to 1.

b) Rate, including equilibrium limitation:

$$R_{c_7} = \frac{R_{c_7}^+}{y_4^2}\left(y_4^2 - \frac{y_5}{K_{E_7}}\right) .$$

The equilibrium relation assumes $|a_{4,7}| \cong 2$.

c) Overall rate, including mass transfer limitation.

(1) If $y_4^2 - (y_5/K_{E_7}) > 0$ (i.e., forward reaction), then:

$$R_7 = \frac{1}{(1/R_{c_7}) + (2/k_y y_4)} .$$

Here we assume $|a_{4,7}| \cong 2$.

(2) If $y_4^2 - (y_5/K_{E_7}) < 0$ (i.e., reverse reaction), then:

$$R_7 = \frac{1}{(1/R_{c_7}) + (1/-k_y y_5)} .$$

8. Water-gas shift reaction.

R_8: $CO + H_2O(g) \rightleftharpoons CO_2 + H_2$

a) Base chemical rate:

$$R_{c_8}^+ = 3 \times 10^7\ \phi\ C_3\ C_6\ \exp\left(\frac{-7250}{\tilde{T}_2}\right).$$

The form of this rate expression was assumed. The magnitude of the pre-exponential constant is a result of consideration of the data from Ref. 6 (and consideration of the stable numerical calcula-

tion). The activation energy term is derived from temperature dependence of the data in the same reference.

b) Rate, including equilibrium limitation:

$$R_{c_8} = \frac{R^+_{c_8}}{C_3C_6}\left[C_3C_6 - \frac{C_4C_7}{K_{E_8}}\right].$$

c) Overall rate, including mass transfer limitation.

(1) If $C_3C_6 - (C_4C_7/K_{E_8}) < 0$ (i.e., forward reaction), then:

$$R_8 = \frac{1}{(1/R_{c_8}) + (1/k_y y_6)}.$$

(2) If $C_3C_6 - (C_4C_7/K_{E_8}) < 0$ (i.e., reverse reaction), then:

$$R_8 = \frac{1}{(1/R_{c_8}) + (1/-k_y y_7)}.$$

9. Gas-phase oxidation reactions.

R_9: $2H_2 + O_2 \rightarrow 2H_2O$

R_{10}: $2CO + O_2 \rightarrow 2CO_2$

R_{11}: $CH_4 + 2O_2 \rightarrow 2H_2O$

Because the kinetics of the gas phase oxidation reactions are, in reality, determined by wall effects (chain terminations), they are handled here in a somewhat arbitrary fashion. (If they are found to be important, it will be necessary to improve the present specification). Currently, two possibilities exist. They are (1) all rates may be set to 0, eliminating the gas-phase oxidation reactions, or (2) one of the three reactions can be given a nonzero rate according to the following expression:

$T_g \leqslant T^+$, $R_I = 0$, where T^+ is an assumed ignition temperature,

$T^+ < T_g\ T^+ + 200$, $R_I = R^+[(T_g - T^+)/200]$,

$T^+ + 200 \leqslant T_g$, $R_I = R^+$, with $R^+ = \beta(dv/dx)C_\ell$.

Here C_ℓ is the concentration of the limiting reactant (usually O_2) and β is a fractional consumption per unit calculated cell (usually 0.1). This merely represents a *very* fast reaction going to completion in a manner that is consistent with finite-difference numerical calculations.

APPENDIX D
CHAR THERMODYNAMICS

Equilibrium constants are required at a given temperature and pressure for each reaction involving coal char and several common gas species. The basic thermodynamic information required for each species is the heat of formation and absolute entropy at 298 K, and the heat capacity from 298 K to the temperature of interest. For the gaseous species, these data are available in the JANAF[16] tables. For coal char, however, the thermodynamic functions must be estimated.

Representing char as $CH_{\bar{a}}O_{\bar{b}}$, the following empirical relations are used:

$$\Delta H^{\circ}_{f,298} = \begin{matrix} 0 \\ 2.6 - 68.0b \end{matrix} ; \quad \begin{matrix} \bar{a} = 0 \\ \bar{a} > 0 \end{matrix} \quad \text{(kcal/mole)}, \tag{D-1}$$

$$S^{\circ}_{298} = 1.359 + 3.17a + 4.0b \quad \text{(cal/g-mole·K)}, \tag{D-2}$$

$$C_p(T) = C_p\,(T,\text{graphite}) + .88\bar{a} + 5.8\bar{b} \quad \text{(cal/g-mole·K)}. \tag{D-3}$$

Equation D-1 for the heat of formation, with $\bar{a} > 0$, is based on the Dulong formula[17] for the heat of combustion of coal. The formula is simply back-solved for the heat of formation of char, knowing the heats of formation of carbon dioxide and liquid water. The Dulong formula has been found by Thibaut[18] to work well for cokes containing varying amounts of hydrogen, $\bar{a}$, and oxygen, $\bar{b}$. To generate the quoted heat of formation of amorphous carbon, 2600 kcal/mole, we set $\bar{a} \approx 10^{-6}$ and $\bar{b} = 0$ in Eq. D-1. To generate graphite with a zero heat of formation, we set $\bar{a} = \bar{b} = 0$.

Equation D-2 for the absolute entropy of coal char comes from a correlation due to Krikorian[19] based on the entropies of high molecular weight, solid, aromatic hydrocarbons. For $\bar{a} = \bar{b} = 0$, the entropy reduces to the value for graphite.

Equation D-3 for char heat capacity is essentially a Kopp's Law additive atomic component relation, except that the carbon component is assumed to have the normal graphite temperature dependence. For graphite, we use a polynomial in the temperature which accurately represents the JANAF[16] tables from 298-2000 K. We have taken the Kopp's Law coefficients for hydrogen and oxygen from Gomez et al.,[20] who determined these from a variety of British coals at room temperature. Over a temperature range 300-2000 K, the heat capacity of graphite increases by almost a factor of 3, while hydrogen and oxygen increase only about 20%. It therefore seems reasonable that the heat capacity of a char should follow the graphite temperature curve with small, essentially temperature-independent corrections due to the hydrogen and oxygen present. This procedure is consistent with the findings of Kirov and Stephens.[21] Equation D-3 gives a plausible heat capacity estimate over a wide temperature range, unlike the equations given in either Refs. 20 or 21, which give unreasonable results at higher temperatures.

It should be clear from the discussion above that our scheme for char thermodynamics is quite approximate and based on very limited data. One use for the formalism is to explore the sensitivity of calculated equilibrium results to the hydrogen and oxygen content of the char. Table D-1 shows calculated results for carbonaceous solids ranging from graphite to a low temperature char with a high hydrogen and oxygen content. The calculations have been carried out both with and without methane in the equilibrium gas.

With methane present, there is a marked increase in the calculated heating value of the equilibrium gas as the hydrogen and oxygen content of the char increase. There is also a large decrease in the oxygen requirement (moles O_2 required/mole solid consumed) as a and b increase. The differences between grahite and amorphous carbon stem from the finite heat of formation of amorphous carbon. With methane suppressed, the calculated heating values are reduced and the sensitivity to the char hydrogen and oxygen is diminished.

Table D-1. Calculated equilibrium properties of a carbonaceous solid, CH_aO_b, at 1000 K, 3 atm, with a steam/oxygen molar feed ratio = 2.

Solid	a	b	mole O_2 / mole solid	Composition (mole %)					Heating Value
				CO	CO_2	H_2	CH_4	H_2O	(Btu/scf)
equilibrium methane									
graphite	0	0	0.38	37	21	28	2	12	260
amorphous carbon	10^{-6}	0	0.29	53	13	24	6	4	320
high temperature char	0.15	0.02	0.23	62	6	19	12	1	380
low temperature char	0.40	0.10	0.17	69	1	8	21	1	460
methane suppressed									
graphite	0	0	0.40	35	21	31	–	13	240
amorphous carbon	10^{-6}	0	0.32	51	11	33	–	5	280
high temperature char	0.15	0.02	0.27	57	5	36	–	2	300
low temperature char	0.40	0.10	0.23	60	1	39	–	–	310

APPENDIX E
VARIABLE ZONING

The grid network used in the problem solution consists of subdivisions of four types of unchanging major zones. The four types of zones are shown in Fig. E-1. They are:

- Type 1 zones which have no internal subdivision of the major zone Δx_ℓ.
- Type 2 zones which are transition zones between type 1 and type 3 zones in the flow direction. They divide the major zone into several subzones. Each subzone has a length which is an integer multiple of Δx_s.
- Type 3 zones which are the finest subdivision of the major zones. Each subdivision is the same size Δx_s.
- Type 4 zones are the same as type 2 zones, only they correspond to a transition from type 3 to type 1 zones in the flow direction.

The nodal points represented by X's are always retained during the solution. The internal divisions change with time. Newly created X points represent given values for T_s, P, and ρ_i using linear interpolation and are based on the X's two nearest neighbors.

A series of tests, performed after each successful time step (or series of time steps), determines if a new grid system is needed. These tests determine whether or not a major zone X_L (each major zone is associated with its downstream boundary node) is to change from a nontype 3 zone to a type 3 zone, or vice versa. Rate, temperature, and pressure criteria determine these changes.

Rate Criteria

Change zone X_L from a nontype 3 zone to a type 3 zone if

$$R_i\Big|_{x_j} \geqslant R^* = \frac{\omega_1 G}{\Delta x_\ell}\Bigg|_{x=0,\ t=0} \qquad (\omega_1 \cong 0.02)$$

for any $X_l \leqslant x_j < X_{L+1}$. Here G is the molar feed rate into the bed.

Change zone X_L from a type 3 zone to a nontype 3 zone if

$$R_i\Big|_{x_j} < \omega_2 R^* \qquad (\omega_2 \cong 0.7)$$

for all $X_L \leqslant x_j < X_{L+1}$.

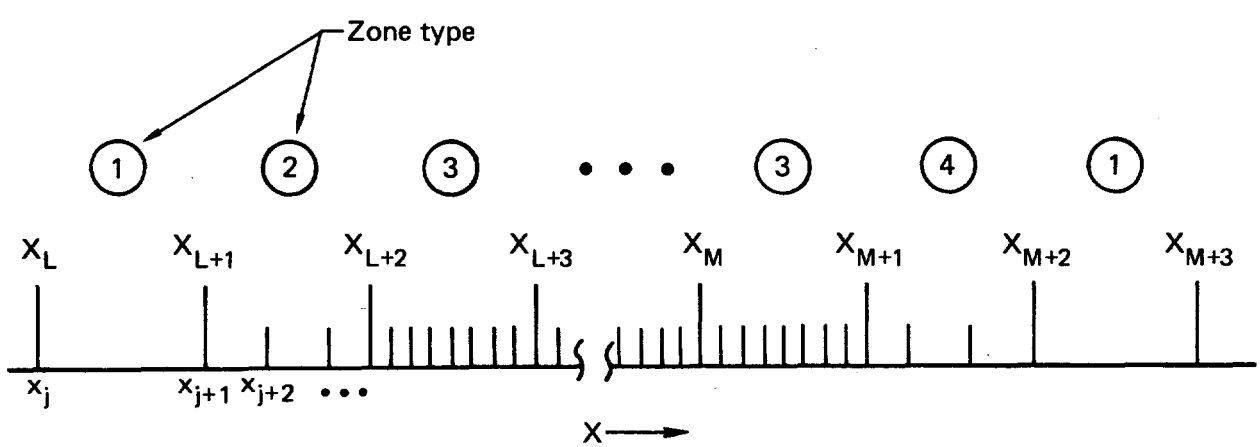

Fig. E-1. A typical portion of the grid system used in the numerical solution.

Temperature Gradient Criteria

Change zone X_L from a nontype 3 zone to a type 3 zone if

$$\left| \frac{T_s\big|_{x_j} - T_s\big|_{x_{j-1}}}{x_j - x_{j-1}} \right| \geqslant \frac{\Delta T^*}{\Delta x_\ell} \qquad (\Delta T^* \cong 40K)$$

for any set $X_L \leqslant x_j < X_{L+1}$ and $X_L \leqslant x_{j-1} < X_{L+1}$.

Change zone X_L from a type 3 to a nontype 3 if

$$\left| \frac{T_s\big|_{x_j} - T_s\big|_{x_{j-1}}}{x_j - x_{j-1}} \right| < \omega_2 \frac{\Delta T^*}{\Delta x_\ell}$$

for all members of the set $X_L \leqslant x_j < X_{L+1}$ and $X_L \leqslant x_{j-1} < X_{L+1}$.

Pressure Criteria

Make zone X_L type 3 if

$$\frac{P\big|_{X_{L+1}} - P\big|_{X_L}}{P\big|_{X_L}} \geqslant P^* \quad (P^* \cong 0.05).$$

The exact size of ω_1, ΔT^*, and P^* can be changed to fit the problem; however, those values in parentheses have been found to be satisfactory to date.

After using the above criteria to determine if a zone is to be type 3, type 2 and 4 zones are inserted to maintain the pattern 1234123.... In the 1234 pattern, 1's and 3's may be repeated in adjacent zones. A single nontype 3 zone is never created in the middle of two type 3 zones. To prevent this happening, the change criteria are overridden and this entire zone is set to a type 3.

The specification of the exact form of type 3 zones is accomplished simply by the specification of the number of fine subdivisions. Type 1 zones are characterized by the specification of Δx_ℓ. The type 2 and type 4 zones are specified by the number of subdivisions and the size of each subdivision is given as a multiple of Δx_s.

APPENDIX F
FINITE DIFFERENCE REPRESENTATIONS

Gas-Phase Equations in Large Zones

The general set of equations below is used in the coarse zones to obtain a solution at the j+1 space location. All variables are given at the current time level. The tildes represent estimated values. For C_i where i = 1, 2, 4, 5, 7, or 8, use Eq. F-3. The equations, given in the order solved, are:

$$C_{6_{j+1}} = \left\{ \frac{C_{6_j}}{\Delta x_j} + \frac{1}{v_{\widetilde{j+1}}} \left[\sum_{k=1}^{11} a_{6,k} R_k + a_{6,8} \left. \frac{\partial R_8}{\partial C_6} \right|_{\widetilde{j+1}} C_{6_{\widetilde{j+1}}} \right] \right\}$$

$$\left\{ \frac{1}{\Delta x_j} + \frac{1}{v_{\widetilde{j+1}}} \left[\frac{v_{\widetilde{j+1}} - v_j}{\Delta x_j} + a_{6,8} \left. \frac{\partial R_8}{\partial C_6} \right|_{\widetilde{j+1}} \right] \right\}^{-1}, \qquad \text{(F-1)}$$

$$C_{3_{j+1}} = \left\{ \frac{C_{3_j}}{\Delta x_j} + \frac{1}{v_{\widetilde{j+1}}} \left[\sum_{k=1}^{11} a_{3,k} R_k + C_{3_{\widetilde{j+1}}} \right.\right.$$

$$\left.\left. \times \left(a_{3,1} \left. \frac{\partial R_1}{\partial C_3} \right|_{\widetilde{j+1}} + a_{3,2} \left. \frac{\partial R_2}{\partial C_3} \right|_{\widetilde{j+1}} \right) \right] \right\}$$

$$\left\{ \frac{1}{\Delta x_j} + \frac{1}{v_{\widetilde{j+1}}} \left[a_{3,1} \left. \frac{\partial R_1}{\partial C_3} \right|_{\widetilde{j+1}} + a_{3,2} \left. \frac{\partial R_2}{\partial C_3} \right|_{\widetilde{j+1}} \right] + \frac{(v_{\widetilde{j+1}} - v_j)}{\Delta x_j} \right\}^{-1}, \qquad \text{(F-2)}$$

$$C_{i_{j+1}} = \left\{ \frac{C_{i_j}}{\Delta x_j} + \frac{\sum_{k=1}^{11} a_{i,k} R_k}{v_{\widetilde{j+1}}} \right\} \left\{ \frac{1}{\Delta x_j} + \frac{v_{j+1} - v_j}{\Delta x_j} \right\}^{-1}, \qquad \text{(F-3)}$$

$$T_{j+1} = \left\{ \frac{T_j}{\Delta x_j} + \frac{1}{v_{j+1}\, c_g} \left(h_T\, T_{s_{j+1}} - H_g \right) \right\} \left\{ \frac{1}{\Delta x_j} + \frac{h_1}{v_{j+1}\, c_g} \right\}^{-1}, \qquad \text{(F-4)}$$

$$\Delta x_j = x_{j+1} - x_j \,. \qquad \text{(F-5)}$$

The coefficients c_g and h_T are evaluated at x_{j+1} position. After solving Eq. F-1, R_8 is redefined by adding the term due to the linearization. This is also done for R_3 after solution of Eq. F-2.

Solid Phase Equations

The finite difference forms used to solve for T_s and the n+1 time level are given below. The subscripts j−1, j, and j+1 refer to adjacent space locations. All coefficients and source terms are evaluated at the x_j location. The tildes represent the current estimated values. The forms are

$$\frac{c_s^n\left[T_{s_j}^{n+1} - T_{s_j}^n\right]}{\Delta t} = \left\{\frac{2}{\Delta x_j^2\,\Delta x_{j-1} + \Delta x_j\,\Delta x_{j-1}^2}\right\}\left\{\left[K_2\,\Delta x_{j-1}\right]\right.$$

$$\left. \times\; T_{s_{j+1}}^{n+1} - \left[K_2\,\Delta x_{j-1} + K_1\,\Delta x_j\right] T_{s_j}^{n+1} + \left[K_1\,\Delta x_j\right] T_{s_{j+1}}^{n+1}\right\}$$

$$+\; h_T^n\left(\widetilde{T_j^{n+1}} - T_{s_j}^{n+1}\right) - \left(V_{w_j}\,\rho_{3_j}\right)^{\widetilde{n+1}}\left[\frac{T_{s_{j+1}}^{n+1} - T_{s_{j-1}}^{n+1}}{\Delta x_{j-1} + \Delta x_j}\right]$$

$$-\,\widetilde{H_{s_j}^{n+1}} - \left[\Delta H_1 \left.\frac{\partial R_1}{\partial T_s}\right|_j^{\widetilde{n+1}} + \Delta H_2 \left.\frac{\partial R}{\partial T_s}\right|_j^{\widetilde{n+1}}\right]\left[T_{s_j}^{n+1} - \widetilde{T_{s_j}^{n+1}}\right] \qquad \text{(F-6)}$$

where $K_1 = \dfrac{\widetilde{k_j^{n+1}}\,(1 - \widetilde{\phi_j^{n+1}}) + \widetilde{k_{j-1}^{n+1}}\,(1 - \widetilde{\phi_{j-1}^{n+1}})}{2}$ and $K_2 = \dfrac{\widetilde{k_{j+1}^{n+1}}\,(1 - \widetilde{\phi_{j+1}^{n+1}}) + \widetilde{k_j^{n+1}}\,(1 - \widetilde{\phi_j^{n+1}})}{2}$.

After four iterations, the coefficients c_s, K_1, K_2, h_T, and $V_w\rho_3$ are not reevaluated.

For the special case j = 1, which corresponds to x = 0, we have:

$$\frac{\widetilde{c_s^{n+1}}}{\Delta t}\left[T_{s_1}^{n+1} - T_{s_1}^n\right] = \frac{2\widetilde{k_1^{n+1}}\,(1 - \phi_1^n)}{\Delta x_1^2}\left[T_{s_2}^{n+1} - T_{s_1}^{n+1}\right]$$

$$+\,\widetilde{h_T^{n+1}}\left[T_{g_1} - T_{s_1}^{n+1}\right] - \widetilde{H_{s_1}^{n+1}}$$

$$-\left[\Delta H_1 \left.\frac{\partial R_1}{\partial T_s}\right|_1^{\widetilde{n+1}} + \Delta H_2 \left.\frac{\partial R_2}{\partial T_s}\right|_1^{\widetilde{n+1}}\right]\left[T_{s_1}^{n+1} - \widetilde{T_{s_1}^{n+1}}\right]. \qquad \text{(F-7)}$$

For j = J, which corresponds to x = L, we have:

$$\frac{\widetilde{c_s^{n+1}}}{\Delta t}\left[T_{s_j}^{n+1} - T_{s_j}^{n}\right] = -2(1-\widetilde{\phi_{J-1}^{n+1}})\,\widetilde{k_{J-1}^{n+1}}\,\frac{\left[T_{s_j}^{n+1} - T_{s_{J-1}}^{n+1}\right]}{\Delta x_{J-1}^2}$$

$$+ \widetilde{h_T^{n+1}}\left[T_{g_J} - T_{s_J}^{n+1}\right] - \widetilde{H_{s_j}^{n+1}}$$

$$- \left[\Delta H_1 \left.\frac{\partial R_1}{\partial T_s}\right|_J^{\widetilde{n+1}} + \Delta H_2 \left.\frac{\partial R_2}{\partial T_s}\right|_J^{\widetilde{n+1}}\right]\left[T_{s_J}^{n+1} - \widetilde{T_{s_J}^{n+1}}\right] . \quad \text{(F-8)}$$

The solid species balance for mobile water, ρ_3, is for $2 < j < J$:

$$\frac{\rho_{3_j}^{n+1} - \rho_{3_j}^{n}}{\Delta t} = 18\, a_{s_{3,1}}\, \widetilde{R_{1,j}^{n+1}} - \frac{\widetilde{V_w^{n+1}}\left(\rho_{3_{j+1}}^{n+1} - \rho_{3_{j-1}}^{n+1}\right)}{\Delta x_{j-1} + \Delta x_j} . \quad \text{(F-9)}$$

For the special case of j = J, we have:

$$\frac{\rho_{3_J}^{n+1} - \rho_{3_J}^{n}}{\Delta t} = 18\, a_{s_{3,1}}\, \widetilde{R_{1,J}^{n+1}} - \frac{\widetilde{V_w^{n+1}}\left(\rho_{3_J}^{n+1} - \rho_{3_{J-1}}^{n+1}\right)}{\Delta x_{J-1}} . \quad \text{(F-10)}$$

Equations F-9 and F-10 are solved after Eqs. F-6–F-8, and the reaction terms are updated to include the contribution from the linear forms used in Eqs. F-7 and F-8.

The other solid species' balances, for ρ_i where i = 1, 2, 4, or 5, are:

$$\frac{\rho_{i_j}^{n+1} - \rho_{i_j}^{n}}{\Delta t} = M_i \sum_{j=1}^{1} a_{s_{i,k}}\, \widetilde{R_k^{n+1}} . \quad \text{(F-11)}$$

TEST PROBLEMS

Two test problems were run using modified versions of the computer code. The code modifications deleted portions of the program so that it conformed more closely with the simple test problems. As a result, these problems tested only certain portions of the coding. The two problems were a simple heat wave calculation with no chemical reaction and a catalyst regeneration with a single reaction. Results from the computer code and certain analytic solutions are given below.

Heat Wave

This problem calculated the temperature history of a packed bed at some initial temperature T_0 which resulted from the continuous injection of an inert gas at temperature T_i. The code was modified for this problem by holding constant the gas and solid heat capacities and the solid conductivity. The inert gas used was N_2. The important input variables used are given in Table G-1.

Approximate closed-form solutions are available for this problem when we assume that the gas and solid have the same temperature at each point in space. Under this condition, the mathematical statement of the problem assuming constant properties becomes

$$\frac{\partial T}{\partial t} + \omega \frac{\partial T}{\partial x} = \lambda \frac{\partial^2 T}{\partial x^2} ,$$

where $\omega = \dfrac{G\bar{C}_P}{C_{s_1}\rho_1}$ and $\lambda = \dfrac{k}{C_{s_1}\rho_1}$.

An asymptotic solution for this problem, for the boundary conditions:

$$x = L \qquad \frac{dT}{dx} = 0 ,$$

and

$$x = 0 \qquad \omega T - \lambda \frac{\partial T}{\partial x} = \omega T,$$

can be obtained from solution given by Brenner[22] for diffusive mass flow in a bed. The solution is

$$T = T_0 + \Delta T \left\{ \frac{1}{2} \operatorname{erfc}\left[\left(\frac{P}{\tau}\right)(x - \tau)\right] + \left(\frac{4P\tau}{\pi}\right)^{1/2} \right.$$

$$\exp\left[-\frac{P(x-\tau)^2}{\tau}\right] - \frac{1}{2}\left[1 + 4P(x+\tau)\exp(4px)\right]$$

$$\operatorname{erfc}\left[\left(\frac{P\tau}{\pi}\right)^{1/2}(x+\tau)\right] + 2\left(\frac{4P\tau}{\pi}\right)^{1/2}(1 + P\Gamma)$$

$$\exp\left(4P - \frac{P\Gamma^2}{\tau}\right) - 2P(2\Gamma + \tau + 2P\Gamma^2)$$

$$\left. \exp(4P) \operatorname{erfc}\left[\left(\frac{P}{\tau}\right)^{1/2}\Gamma\right] \right\} ,$$

Table G-1. Variables for heat wave problem.

Variable	Value
G (gas flow)	$1 \times 10^{-4} \frac{\text{g-mole}}{\text{s}\cdot\text{cm}^2}$
$\overline{c_p}$	$7 \frac{\text{cal}}{\text{g-mole}\cdot\text{K}}$
T_0	600 K
ρ	$0.9 \frac{\text{g}}{\text{cm}^3}$
ϕ	0.5
c_{s_2}	$0.3 \frac{\text{cal}}{\text{g}\cdot\text{K}}$
k	$0.0025 \frac{\text{cal}}{\text{s}\cdot\text{K}\cdot\text{cm}}$
T_{s_0}	300 K
d (particle diameter)	1 cm
Δt (time step)	20 s
Δx_s (space step)	0.4 cm
L (bed length)	50 cm

where $\Delta T = T_i - T_0 = 300$ K, $P = (\omega L/4\lambda) = 3.03$, $\tau = (t\omega/L)$, $x = (x_d/L)$ (x_d is the dimensional length), and erfc (γ) = complimentary error function of γ. This solution is applicable for P and τ.

A comparison of the above expression with the calculated solid and gas temperatures generated by the code for a 50 cm bed 10,000 seconds after injection of gas is given in Fig. G-1. The value of k used is the analytic expression, which was modified using:

$$k = k(\text{solid}) + \frac{(GC_g)^2}{h_T} ,$$

$$k = 0.0029 \frac{\text{cal}}{\text{s}\cdot{}^{\circ}\text{C}\cdot\text{cm}} .$$

This relation, given by Vortmeyer and Schaefer[23] allows the heat transfer coefficient of a two-temperature model to be related to an effective diffusive term of a one-temperature model. The numeric solution agrees fairly well with the analytic result with the largest discrepancy occurring near the inlet end of the system. The maximum deviation related to overall temperture change is 1.5%.

This deviation is at least partly due to two factors. First, the asymptotic solution is recommended for $\tau < 1$ (@ t = 10,000, $\tau = 0.5$) and for $P > 4$. At $P = 3$ and $\tau = 0.5$, it is pushing its range of validity. Second, the boundary conditions used in the numeric solution, $dT_s/dx = 0$ for the solid at $x = 0$ and $T = T_0$ for the gas, are different than those corresponding to the Brenner solution, which, for a two- temperature model (according to Vortmeyer and Schaefer[23]) is:

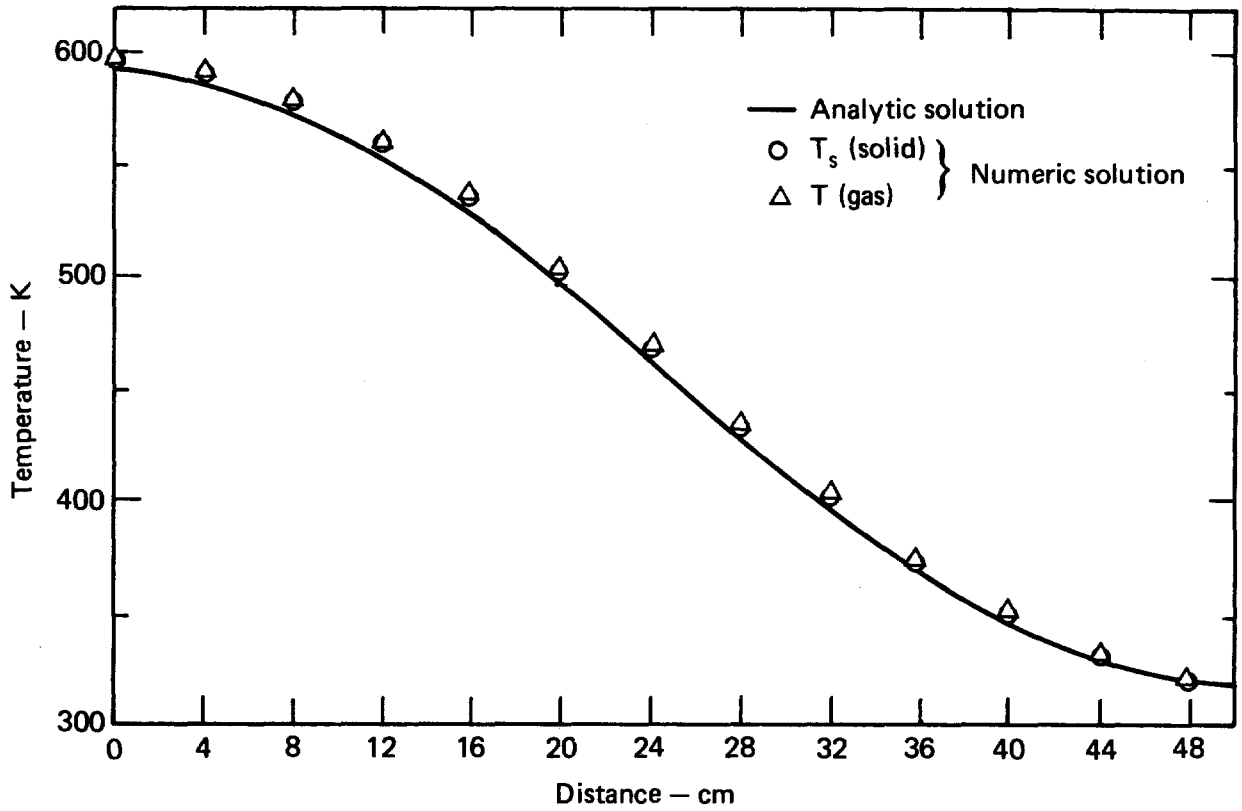

Fig. G-1. A comparison of analytically and numerically calculated temperature profiles for a heat wave problem.

$$GC_g(T_i - T) = (1 - \phi)\, h\, (T_i - T_s)$$

and

$$-k \frac{dT_s}{dx} = (1 - \phi)\, h\, (T_i - T_s).$$

This allows heat transfer between gas and solid at the inlet face of the system. Note that these boundary conditions reduce to those used on the numeric code when $T_s \rightarrow T_0$ at $x = 0$. When all the above factors are considered, we conclude that the portions of the code concerned with this calculation are doing an adequate job.

Catalyst Regeneration

This problem calculated the regeneration of a catalyst bed by oxidation of contaminants. The problem was idealized to the following: a packed bed containing a small fraction of carbon by weight initially at temperature T_0 and a gas containing oxygen admitted to the inlet end of the bed at time 0. The required solution developed temperature, oxygen concentration, and carbon concentration through the bed.

The computer model was modified to calculate the required solution by setting all rates to 0 except the $C + O_2 \rightarrow CO_2$ reaction. The input variables used in the test calculation are given in Table G-2.

A closed-form solution for this problem was developed by Johnson et al.[24] in which they neglected conductivity, assumed constant physical properties, assumed equal gas and solid temperatures, assumed adiabatic operation, and used a rate of carbon reaction that can be interpreted for a later system as $R_4 = k\, y_{O_2}\, \rho_c$. Here k is a rate constant that is independent of temperature. The expressions for oxygen and carbon concentration as a function of space and time given by Johnson et al.[24] are

Table G-2. Variables for catalyst regeneration problem.

Variable	Value
G (gas flow)	$4 \times 10^{-4} \frac{\text{g-mole}}{\text{s}\cdot\text{cm}^2}$
y_{O_2}	0.02
y_{N_2}	0.98
$\overline{c_p}$	$\sim 7 \frac{\text{cal}}{\text{g-mole}\cdot\text{K}}$
T_i	600 K
ρ_c (carbon concentration)	0.0107
ρ_{ash} (inert concentration)	1.482
ϕ	0.5
k	$0.0025 \frac{\text{cal}}{\text{s}\cdot\text{K}\cdot\text{cm}}$
$\overline{c_s}$	$\sim 0.21 \frac{\text{cal}}{\text{g}\cdot\text{K}}$
T_0	600 K
d	1 cm
L	40 cm
Δx_s	0.2 cm
Δt	10 s
k_r (rate constant)	($0.00472\ s^{-1}$)
M_y (average molecular weight of gas)	28.3
Q (heat release per mole of CO_2)	$96700 \frac{\text{cal}}{\text{mole}}$

$$\left.\frac{y_{0_2}}{y_{0_2}}\right|_{t=0} = \frac{1}{1 + e^{-\tau}(e^{\xi} - 1)}$$

$$\left.\frac{\rho^c}{\rho^c}\right|_{t=0} = \frac{1}{1 + e^{-\xi}(e^{\tau} - 1)}$$

where:

$$\xi = x\left(\frac{k_r \rho^c \big|_{t=0}}{G}\right)$$

$$\tau = \left(y_{0_2}\Big|_{t=0} 12k_r\right)\left(t - x\,\frac{\phi P}{RTG}\right) .$$

The temperature relation is more complex, but under the special conditions

$$H = \left(\frac{\bar{c}_p \rho_c \big|_{t=0}}{12\bar{c}_s \rho y_{0_2}\big|_{t=0}}\right) = 1$$

$$M = \left[1 - \frac{\bar{c}_p \phi P}{RT\,\bar{c}_s \rho}\right] = 1$$

and all combustion proceeding to CO_2, a closed-form solution was developed by Johnson et al.[24] Their result represented by their Eq. 28 is not valid over the entire range of the independent variables. The current solution is given instead by the following for $\tau \geqslant \xi$,

$$T = T_0 + \Delta T\left\{\frac{e^{\xi-\tau}}{(1 + e^{\xi-\tau})^2}\left[\ell nU - \frac{1}{U}\right]\Bigg|_{U=e^{\xi-\tau}}^{U=e^{\tau} + e^{\xi} - 1}\right\},$$

and for $\xi \geqslant \tau$,

$$T = T_0 + \Delta T\left\{\frac{e^{\tau-\xi}}{(1 + e^{\tau-\xi})^2}\left[\ell nU - \frac{1}{U}\right]\Bigg|_{U=e^{\tau-\xi}}^{U=e^{\tau} + e^{\xi} - 1}\right\}.$$

Here $$\Delta T = \frac{Q\rho_{c_0}}{12\,\bar{c}_s \rho} = 277°C .$$

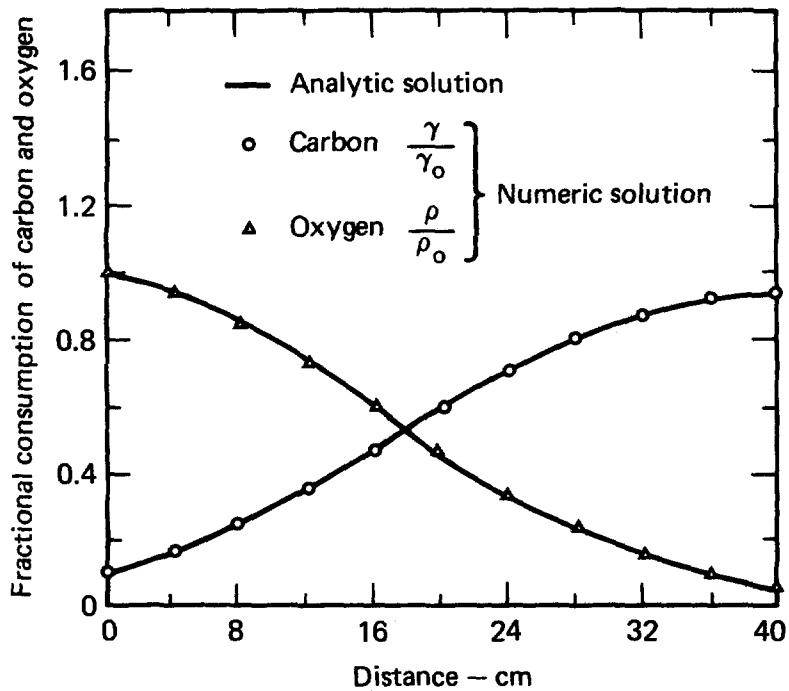

Fig. G-2. A comparison of analytically and numerically calculated concentration and solid density profiles for a regenerator problem.

Figure G-2 shows a comparison of analytic and numeric solutions for the relative oxygen concentration and carbon density after 2000 seconds of operation. The agreement is very good with less than 0.6% difference between analytic and numeric results. This high rate of agreement is expected since the assumptions in the computer model and in the analytic approach are identical with respect to the mathematical formulation and differ only in the method of solution. On the other hand, the mathematical formulation of the heat balance differs in several ways. The analytic approach necessarily makes the following assumptions not made in the numeric solution:

- constant heat capacities,
- constant densities,
- gas and solid temperatures equal,
- no conductivity in the bed.

However, a comparison of temperatures using the two approaches still allows some approximate check to be made on the temperature calculations. Figure G-3 shows this comparison. Note that the primary difference is near the peak temperature. This undoubtedly is a result of the nonzero conductivity in the computer model; other than that, the results seem to compare satisfactorily.

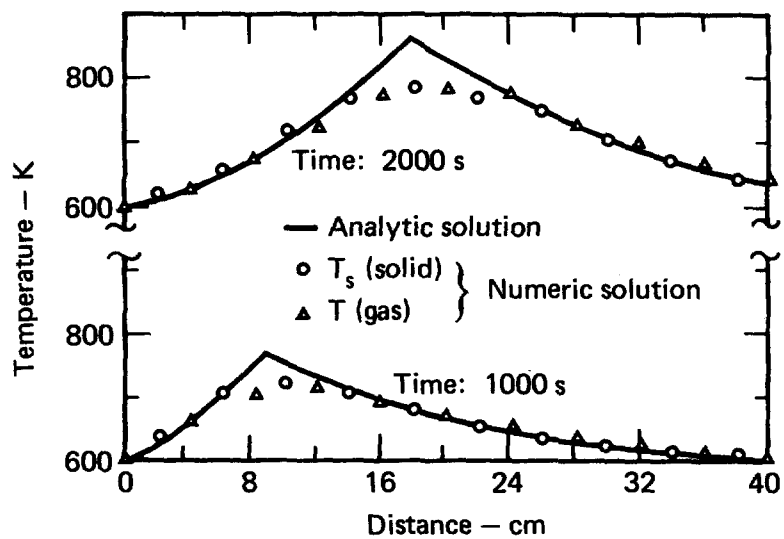

Fig. G-3. A comparison of analytically and numerically calculated temperature profiles for a regenerator problem.

REFERENCES

1. W. K. Sawyer and L. Z. Shuck, "Numerical Simulation of Mass and Energy Transfer in the Longwall Process of Underground Gasification of Coal," Paper SPE 574, presented at the 4th Symposium of Numerical Simulation of Reservoir, Los Angeles, Calif., Feb. 19-20, 1976.
2. A. A. Winslow, *Numerical Model of Coal Gasification in a Packed Bed,* Lawrence Livermore Laboratory, Livermore, Calif., UCRL-77627 (1976).
3. S. Yagi and D. Kunii, "Studies on Effective Thermal Conductivities in Packed Beds," *AIChE J.* 3, (1957) pp. 373-381.
4. R. Bird et al. *Transport Phenomena* (John Wiley & Sons, Inc., New York, 1960), pp. 389-425.
5. G. A. Karim and D. Mohindra, "A Kinetic Investigation of the Water Gas Shift Reaction in Homogenous Systems," *J. of the Inst. of Fuel,* (1974), pp. 219-223.
6. G. B. Grebenshchikova, "Study of the Kinetics of the Conversion of Carbon Monoxide by Steam in the Presence of Ash from Lisichansk Coal," *Podzemnaya Gazifikatsiya Uglei* 2, (1957), pp. 54-57. Also Lawrence Livermore Laboratory Translation, Livermore, Calif., UCRL-TRANS-10900 (1975).
7. J. M. Smith and H. C. Van Ness, *Introduction to Chemical Engineering Thermodynamics,* (McGraw-Hill, New York, 1959), p. 122.
8. R. Vetterlein, "Permeability of Cork-Shaped Coal Samples," Lawrence Livermore Laboratory, Livermore, Calif., private communication (April 1, 1975).
9. E. A. Grens, "Porosity of Coal," Lawrence Livermore Laboratory, Livermore, Calif., private communication (May 8, 1975).
10. J. H. Campbell, *Pyrolysis of Subbituminous Coal as it Relates to In-Situ Gasification (Part 1: Gas Evolution),* Lawrence Livermore Laboratory, Livermore, Calif., UCRL-52035 (1976).
11. R. W. Taylor and D. Bowen, *Rates of Reaction of Steam and Carbon Dioxide with Chars Produced from Subbituminous Coals,* Lawrence Livermore Laboratory, Livermore, Calif., UCRL-52002, (1975).
12. A. B. Newman, "The Drying Porous Solids: Diffusion and Surface Emission Equations," *Trans. AIChE* 27, (1931), p. 203.
13. A. L. Parker and H. C. Hottel, "Combustion Rate of Carbon: Study of Gas-Film Structure by Microsampling," *Ind. Eng. Chem.* 28, (1936), pp. 1334-1341.
14. E. Pyrcioch et al., *Production of Pipeline Gas by Hydrogasification,* Res. Bull. No. 39, Vol. I, Institute of Gas Technology, Chicago, Illinois, (Dec. 1972).
15. C. G. Von Fredersdorff and M. A. Elliott, "Coal Gasification," in *Chemistry of Coal Gasification,* H. H. Lowry, Ed., (John Wiley & Sons, Inc., New York, 1963), pp. 892-1022.
16. Daniel Richard Stull, *JANAF Thermochemical Tables,* 2nd ed., U.S. Government Printing Office, Washington, D.C., 1971.
17. O. A. Hougen and K. M. Watson, *Chemical Process Principles, Past Due,* (John Wiley & Sons, Inc., New York, 1948), p. 327.
18. Ch. G. Thibaut, "Solid Products of Carbonization," in *Chemistry of Coal Gasification,* H. H. Lowry, Ed., (John Wiley & Sons, Inc., New York, 1963), pp. 494-538.
19. O. H. Krikorian, *Thermodynamic Properties of Wyoming Coals,* Lawrence Livermore Laboratory, Chemistry Department Technical Note 72-18, Livermore, Calif., (April 1972).
20. M. Gomez et al., *Heat Content and Specific Heat of Coals and Related Products,* U.S. Bureau of Mines, RI 6607, 1965.
21. N. Y. Kirov and J. N. Stephens, *Physical Aspects of Coal Carbonization,* University of New South Wales Research Monograph, Sydney, 1967.
22. H. Brenner, "The Diffusion Model of Longitudinal Mixing in Beds of Finite Length. Numerical Values," *Chem. E. Sci.* 17, (1962), p. 229.
23. D. Vortmeyer and R. J. Schaefer, "Equivalence of One- and Two-Phase Models for Heat Transfer Processes in Packed Beds: One-Dimensional Theory," *Chem. E. Sci.* 29, (1974), pp. 485-491.
24. B. M. Johnson et al., "Temperature Profiles in Packed Beds of Catalyst During Regeneration," *Chem. E. Sci.* 17, (1962), pp. 835-848.

LJH

Technical Information Department
LAWRENCE LIVERMORE LABORATORY
University of California | Livermore, California | 94550

179 983

VAULT REFERENCE COPY

RECEIVED
LAWRENCE LIVERMORE LABORATORY

NOV 03, 1978

TECHNICAL INFORMATION DEPARTMENT